Available online at www.sciencedirect.com

ScienceDirect

Geochimica et Cosmochimica Acta 326 (2022) 234–252

Geochimica et Cosmochimica Acta

www.elsevier.com/locate/gca

Decoupled Zn-Sr-Nd isotopic composition of continental intraplate basalts caused by two-stage melting process

Rong Xu [a,b], Yongsheng Liu [b,*], Sarah Lambart [c], Kaj Hoernle [d,e], Yangtao Zhu [b], Zongqi Zou [b], Junbo Zhang [b], Zaicong Wang [b], Ming Li [b], Frédéric Moynier [f], Keqing Zong [b], Haihong Chen [b], Zhaochu Hu [b]

[a] State Key Laboratory of Ore Deposit Geochemistry, Institute of Geochemistry, Chinese Academy of Sciences, Guiyang 550081, China
[b] State Key Laboratory of Geological Processes and Mineral Resources, School of Earth Sciences, China University of Geosciences, Wuhan 430074, China
[c] Geology and Geophysics, University of Utah, Salt Lake City, UT, United States
[d] GEOMAR Helmholtz Centre for Ocean Research Kiel, 24148 Kiel, Germany
[e] Kiel University, Institute of Geosciences, 24118 Kiel, Germany
[f] Université de Paris, Institut de Physique du Globe de Paris, CNRS UMR 7154, 75238 Paris Cedex 05, France

Received 30 October 2021; accepted in revised form 11 March 2022; Available online 16 March 2022

Abstract

Ocean island basalts (OIBs) with Zn isotopic ratios higher than the normal mantle ($\delta^{66}Zn = 0.17 \pm 0.08‰$) or mid-ocean ridge basalts (MORBs; $\delta^{66}Zn = 0.27 \pm 0.06‰$) generally also have an enriched Sr-Nd isotopic signature, suggesting carbonate-bearing eclogites, whose protolith is inferred to be subducting altered oceanic crust, in their mantle source. On the contrary, continental intraplate basalts with high $\delta^{66}Zn$ usually show depleted Sr-Nd isotopic signatures (i.e., decoupled Zn-Sr-Nd isotopic composition). To elucidate the origin of the decoupled Zn-Sr-Nd isotopic composition in continental intraplate basalts, we report the discovery of both coupled and decoupled Zn-Sr-Nd isotopic data for a suite of Cenozoic continental intraplate basalts from the Zhejiang province, Southeast China. These basalts display clear spatial and temporal geochemical variations, with early-stage inland low-silica samples presenting moderately enriched Sr-Nd isotopic signatures and high $\delta^{66}Zn$ (coupled Zn-Sr-Nd isotopic composition, similar to OIBs), and later-stage coastal high-silica samples that display a pronounced $\delta^{66}Zn$ decrease with increasing SiO_2 and $^{87}Sr/^{86}Sr$ and with decreasing alkali contents and $^{143}Nd/^{144}Nd$ (decoupled Zn-Sr-Nd isotopic composition). The early-stage basalts with coupled high Zn-Sr-Nd isotopic signatures are also more enriched in incompatible elements than any other basalts from eastern China reported so far. We explain the spatial and temporal geochemical variations of these basalts as the result of two main melting events: 1) the low-silica early-stage magmatism mostly occurs inland and results from high-pressure partial melting of a carbonated eclogite-bearing asthenospheric mantle. Because of the presence of a thick lithosphere limits the melting of the depleted mantle component, the signature of the Zn-Sr-Nd isotopically enriched, and more fusible carbonated eclogite is preserved. 2) At the later stage, magmatism mostly occurs on the coast where the subcontinental lithosphere is thinner. Hence, decompression melting progresses to shallower depth, resulting in an increase of the contribution from the depleted peridotite matrix and a dilution of the signal from the isotopically enriched fusible component. Further upwelling and in-situ melting at the base of the subduction-modified subcontinental lithospheric mantle (SCLM) explains both the decoupled Zn-Sr-Nd isotopic signature of the coastal basalts and their major and trace element variability. We further propose that decompression melting is driven by small-scale convection resulting from variations of lithospheric thickness. Our data highlight the importance of dynamic melting of carbonated eclogite-bearing asthenosphere and subsequent lithospheric melting in preservation and destruction of the coupled enriched

* Corresponding author.
E-mail addresses: rongxu@cug.edu.cn (R. Xu), yshliu@cug.edu.cn (Y. Liu), sarah.lambart@utah.edu (S. Lambart).

https://doi.org/10.1016/j.gca.2022.03.014

Zn-Sr-Nd isotopic signature of carbonated eclogite component and generation of the apparent decoupled Zn-Sr-Nd isotopic signal commonly observed in continental intraplate basalts.

Keywords: Alkali basalt; Zn isotope; Carbonated eclogite-bearing asthenosphere; Subcontinental lithospheric mantle; Small-scale convection

1. INTRODUCTION

Carbonated slabs can be subducted into the deep mantle at convergent margins (Thomson et al., 2016; Beunon et al., 2020). During subsequent mixing and upwelling of the asthenospheric mantle, the carbonated components may reach the mantle source of magmas and be recycled at the surface in the form of intraplate continental or oceanic basalts (Gerbode and Dasgupta, 2010; Castillo, 2015; Xu et al., 2020b). Tracing the recycled carbonated components in the mantle-derived magmas remains a frontier field in the deep carbon cycle research. Because marine carbonates can have significantly higher δ^{66}Zn compared to the mantle (Liu and Li, 2019 and references therein), Zn isotopic ratio has been proven to be a powerful geochemical tool to trace the subducted carbonate or carbonated eclogite in the mantle source of intraplate basalts (Liu et al., 2016a; Wang et al., 2018; Beunon et al., 2020).

In oceanic settings, island basalts (OIBs) with high δ^{66}Zn usually also display an enriched Sr-Nd isotopic signature (i.e., high $^{87}Sr/^{86}Sr$ and low $^{143}Nd/^{144}Nd$). This association of high Zn isotopic ratio and enriched Sr-Nd isotopic signature (hereafter named as a coupled Zn-Sr-Nd isotopic signal) has been interpreted as indicating the presence of carbonate-bearing eclogite in the mantle source, whose protolith is inferred to be the subducted altered oceanic crust (Beunon et al., 2020). During decompression melting of a lithologically heterogeneous mantle, the contribution of the enriched component in the aggregated magma will be progressively diluted by the increasing contribution of the depleted mantle (DMM) as decompression continues (e.g., McGee et al., 2013; Lambart, 2017). Hence, these OIBs form a positive trend in the Zn-Sr isotopic space and a negative trend in the Zn-Nd isotopic space, and low-degree partial melts derived from greater depths are more likely to preserve the geochemical signature of the enriched component (e.g., a carbonated eclogite component) than high-degree melts formed at shallower depths.

Continental intraplate basalts with high δ^{66}Zn exhibit several similarities with high δ^{66}Zn OIBs, such as high incompatible trace element concentrations and low-silica contents. If, similar to OIBs, these characteristics in continental basalts are, in fact, indicators of involvement of carbonate-bearing eclogites in the mantle source (Wang et al., 2018), we should expect continental basalts to also possess coupled Zn-Sr-Nd isotopic signatures. However, these coupled enriched Zn-Sr-Nd isotope ratios have not been observed in continental intraplate basalts so far. Instead, individual suites of continental intraplate basalts usually form negative trends in the Zn-Sr isotopic space and positive trends in the Zn-Nd isotopic space (Liu et al., 2016a; Wang et al., 2018; Wang and Liu, 2021), hereafter referred to as a decoupled Zn-Sr-Nd isotopic signature. The decoupling of δ^{66}Zn from Sr-Nd isotopic signal in continental basalts has been interpreted as a result of mixing of subducted magnesite, a high-pressure phase of carbonate, with DMM, without involving carbonated eclogite (Liu et al., 2016a). Alternatively, like with OIBs, carbonated eclogite may actually be involved in the mantle source of continental basalts and ensuing melting processes could be responsible for the apparent decoupled Zn-Sr-Nd isotope signal. Discriminating between the two models has important implications not only for conjecturing the mobility and fate of subducted carbonates during the carbon cycle but also for providing better constraints on their role in the secular evolution of mantle heterogeneity. Therefore, identifying coupled Zn-Sr-Nd isotopic features in continental basalts is crucial to determine whether the mantle source of continental intraplate basalts contains a carbonated eclogite component and what processes are responsible for the overprinting of its geochemical fingerprint.

In continental areas, there is growing recognition that the lithospheric mantle could also exert a control on the compositional spectrum of the continental intraplate alkali basalts by not only acting as a tectonic lid to terminate the asthenospheric upwelling but also serving as a source component, either by direct melting or by indirect melt-rock reactions (Xu et al., 2005; Pilet et al., 2008; Wang et al., 2018; Guo et al., 2020; Wang and Liu, 2021). Therefore, clarifying the potential role of the lithospheric mantle in magma genesis is crucial for our comprehensive understanding of the origin and melting dynamics of intraplate volcanism. If there is indeed involvement of subcontinental lithospheric mantle (SCLM) material in the genesis of continental intraplate basalts, pressure of melt equilibration should indicate lithospheric depths and a late contribution of the SCLM may overprint the initial geochemical signal of the enriched component (e.g., carbonated eclogite). Testing the validity of this hypotheses requires detailed petrological constraints on the melting pressure and temperature (P-T) conditions and efficient geochemical tracers to discriminate potential carbonated component and SCLM component from other components.

Here, we report analyses performed on two groups of Cenozoic basalts from Zhejiang province, Cathaysia block of SE China, separated by a $\sim$ 5 Ma amagmatic period. The early-stage group is composed of low-silica basalts with a coupled Zn-Sr-Nd isotopic signature. The late-stage group presents slightly higher silica content and decoupled Zn-Sr-Nd isotopic signature. We demonstrate that the occurrence of continental intraplate basalts with both coupled and decoupled Zn-Sr-Nd isotopic signatures is the first direct testimony in favor of the two-stage melting process.

We further use these new data to constrain the P-T conditions of melting, define the various source components and their respective contributions to magmatism and present a petrological model that explains the generation and the spatial and chemical evolution of these continental intraplate basalts.

2. GEOLOGICAL SETTING, SAMPLES AND METHODS

South China is tectonically divided into the Yangtze block in the northwest, and the Cathaysia block in the southeast. These two blocks have been considered as two separate members of the Neoproterozoic Rodinia supercontinent (Li et al., 1995). They are separated by an ophiolitic suture along the Jiangshan-Shaoxing fault (Shu and Charvet, 1996), which has been considered as a collisional zone formed during the early Neoproterozoic, around 900 Ma (e.g., Ye et al., 2007; Li et al., 2009).

The exposed basement in the Yangtze block is mainly Proterozoic with sporadically dispersed Archean TTG (tonalite, trondhjemite, and granodiorite) gneisses, metasedimentary rocks, and amphibolites outcrops (e.g., Gao et al., 1999; Qiu et al., 2000). In contrast, the Cathaysia block dominantly consists of a Neoproterozoic crustal basement with limited Paleoproterozoic granitoids outcrops (e.g., Zhao and Cawood, 2012). In the Paleozoic, the influential tectonothermal events in the Cathaysia block occurred during the late Ordovician-Silurian (the Caledonian event) and the late Permian-Triassic (the Indosinian event) (Wang et al., 2013). Subsequently, Mesozoic subduction of the paleo-Pacific plate under the Eurasian plate resulted in the emplacement of large amounts of siliceous magmatism such as rhyolites and granites (Zhou et al., 2006) and mafic rocks (Zeng et al., 2016; Guo et al., 2021) along the continental margin of South China block. Finally, in the Cenozoic, the tectonic setting switched from convergent to extensional. The extension is generally accepted to be related to the opening of the South China Sea (Tapponnier et al., 1986). The opening started ~ 32 Ma ago during the Oligocene and ceased early Miocene between 20.5 Ma (Barckhausen and Roeser, 2004) and 16 Ma (Taylor and Hayes, 1980, 1983; Briais et al., 1993). At least three hypotheses exist for the opening mechanism of the South China Sea: (1) the India-Eurasia collision (Tapponnier et al., 1982; Briais et al., 1993); (2) slab pull from the subduction of the Pacific plate (Taylor and Hayes, 1980, 1983; Shi and Li, 2012); and (3) extension related to a mantle plume (Fan, 1992). Hybrid models combining these end-member hypotheses have also been proposed (e.g., Cullen et al., 2010).

Early geophysical data suggest that the lithospheric thickness beneath South China increases gradually from the coastline (~80 km) toward the continental interior (~190 km) (Ma and Wu, 1987; An and Shi, 2006). This is confirmed by recent teleseismic body-wave attenuation data which shows that the present lithospheric thickness of South China decreases from the Yangtze block in the northwest (~190 km) to the Cathaysia block in the southeast (~75 km) (Deng et al., 2021). This estimate is also consistent with results from multi-observable probabilistic inversion, seismic waves, receiver functions, electrical conductivity, heat flow data (Yang et al., 2021b and references therein) and thermobarometry performed on xenoliths (Huang and Xu, 2010; Liu et al., 2012).

Cenozoic intraplate alkali basaltic volcanism in South China is spatially dispersed along the NE-oriented lithospheric faults (Fig. 1). Among them, the Zhejiang basalts crop out in the northeastern Cathaysia block. Ar-Ar dating suggests the Zhejiang basalts erupted mainly in the Miocene to Pleistocene (Ho et al., 2003), although the oldest K-Ar age can be up to 41.5 Ma (Zeng et al., 2017). Most of these basalts carried small mantle xenoliths, including spinel and garnet lherzolite, and spinel harzburgite, in Xinchang, and spinel-free dunite, harzburgite, wehrlite, and spinel and garnet lherzolite in Xilong area (e.g., Liu et al., 2012; Lu et al., 2015; Qi et al., 1995; Zhang et al., 2021, 2015). Fertile lithologies such as pyroxenites or hydrous mineral (e.g., amphibole or phlogopite)-bearing peridotites have not been observed in these xenoliths (Liu et al., 2012; Lu et al., 2015; Zhang et al., 2021). Re-Os data indicate the spinel-

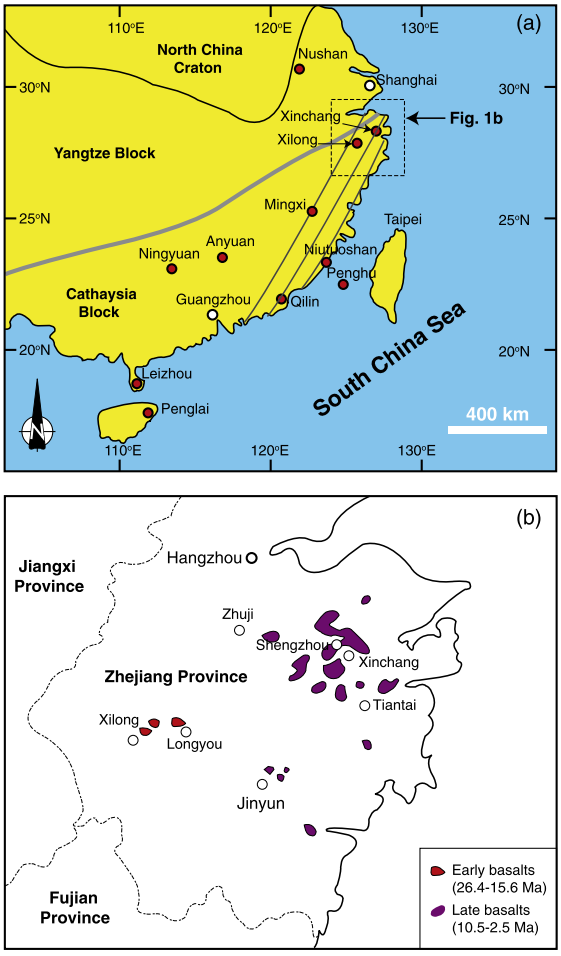

Fig. 1. (a) Simplified tectonic map of SE China, with red circles denote locations of Cenozoic basalts and mantle xenoliths and (b) location of studied Cenozoic basalts in the Zhejiang Province. Modified after Liu et al. (2012).

harzburgites are ancient (Archean or Proterozoic) lithospheric mantle relics, while the lherzolites have younger Os isotope ages and are interpreted as the newly accreted mantle (Liu et al., 2012), supporting the hypothesis that the ancient, cold, thick, and depleted lithospheric mantle has been partly, but not thoroughly, thinned and replaced by a young, hot, and fertile mantle in the Mesozoic.

Based on the Ar-Ar age, the Zhejiang basalts can be divided into two groups (Ho et al., 2003). The early-stage magmatism (Ar-Ar ages of ~ 26–17 Ma) produced small volume of nephelinites and basanites (low-silica group) and was located exclusively in the inland area (inner belt). On the contrary, the late-stage volcanic activity (late-Miocene; < ~11 Ma) erupted voluminous basanites, alkali basalts and tholeiites (high-silica group) closer to the coastal areas (outer belt) (Fig. 1). Ar-Ar data suggest a quiet period of magmatic activity between ~ 17 and ~ 11 Ma (Ho et al., 2003).

A total of 40 samples were collected from Xilong (XL) and Longyou (LY) in the inland area, and from Xinchang (XC), Shengzhou (SZ) and Tiantai (TT) in the coastal area (Fig. 1). We note that although He et al. (2020) reported basalts from Jiande in the inland area with low silica contents and enriched incompatible trace element features, these basalts have undergone significant surface alteration (LOI = 5.22 – 7.92 wt.%; He et al., 2020) that likely affected their Zn isotopic composition (Suhr et al., 2018). Therefore, we excluded the Jiande basalts from our study. Recent geochemical studies showed that the evolved basalts (e.g., samples with MgO < ~8 wt.% and SiO_2 > ~47.5 wt.%) in the Zhejiang area have suffered a complex evolutionary history involving crustal contamination, fractional crystallization and magma recharge (Yu et al., 2015, 2017). Hence, during the field campaign in 2018, we targeted primitive MgO-rich samples (mostly with MgO > ~8 wt.% and SiO_2 < ~47.5 wt.%) following the previously reported GPS coordinates (Yu et al., 2015; Liu et al., 2016b). The collected samples are mainly nephelinites, basanites and alkali basalts. Phenocrysts are mainly composed of euhedral olivine and clinopyroxene, with an overall higher proportion of clinopyroxene phenocrysts in samples from Xinchang and Shenzhou than in samples from Xilong. Dominant groundmass phases are clinopyroxene, Fe-Ti-oxide and olivine (Ho et al., 2003; Li et al., 2015; Liu et al., 2016b).

Major element and Sr-Nd isotopic compositions of whole rocks were measured by X-ray fluorescence (XRF) instrument (Shimadzu XRF-1800) and multi-collector inductively coupled plasma-mass spectrometry (MC-ICP-MS), respectively, at the Wuhan Sample Solution Analytical Technology Co., Ltd. Trace element and Zn isotopic analyses were performed on an Agilent 7500a ICP-MS and a Nu Plasma 1700 MC-ICP-MS instrument, respectively, at the State Key Laboratory of Geological Processes and Mineral Resources (GPMR), China University of Geosciences (Wuhan), China. Analyses of secondary standards show that the relative error for most trace elements is below 5%, and ~ 10% for Ni, Pb, Cr, and Zn. In addition, Sr-Nd and Zn isotopic analyses on the same standards are consistent with previous studies and recommended values within the analytical error (0.002‰ and 0.05‰, respectively). Details of analytical methods can be found in Supplementary Text S1.

3. RESULTS

3.1. Major and trace elements

Bulk rock major and trace element compositions are provided in Supplementary Tables S1 and S2. All of our samples have high MgO (7.9–13.8 wt.%) and total alkalis (3.9–7.4 wt.% $Na_2O + K_2O$) contents (Fig. 2a). Samples from the inland area (XL and LY) have lower silica and higher alkali contents than samples from the eastern nearshore areas (XC, SZ, and TT). In the following discussion, we distinguish these two groups of samples as low- and high-silica samples, respectively.

SiO_2 is negatively correlated with several major and minor element concentrations (MgO, Ni, and Cr; Fig. 2b & Supplementary Fig. S1), with CaO/Al_2O_3 ratios, and with incompatible trace element concentrations (e.g., Sr and Dy; Supplementary Fig. S1). There is a positive correlation between SiO_2 and Sc for SiO_2 < 48 wt.% (Fig. 2c). The three silica richest samples from Shengzhou (SZ) show, however, slightly lower Sc contents. SiO_2 also correlates negatively with ratios of "more to less" incompatible trace elements (e.g., Dy/Yb; Fig. 2d), and with ratios of elements with similar bulk partition coefficients (e.g., Ce/Pb; Supplementary Fig. S2a). Finally, there is a positive correlation between SiO_2 and ratios of fluid-mobile to less fluid-mobile incompatible elements (e.g., K/La; Supplementary Fig. S2b).

All samples show enrichment in highly to moderately incompatible elements with a pronounced peak at Nb and negative anomalies for Pb, Zr, Hf and Ti in the primitive mantle-normalized trace element diagram (Fig. 3). With decreasing silica content, the Nb peak and the K, Pb and Ti negative anomalies become more pronounced, while the Sr peak tones down. Specifically, the low-silica samples from Xilong have the highest incompatible element contents (e.g., Nb) among all of the Cenozoic basalts in eastern China reported so far (see compilation in Xu et al., 2020b).

3.2. Sr-Nd isotopes

Sr–Nd isotopic compositions are listed in Table S3. The $^{87}Sr/^{86}Sr$ and $^{143}Nd/^{144}Nd$ compositions of our samples range from 0.703280 to 0.704271 and 0.512884 to 0.513009, respectively. Samples from Xinchang and Tiantai (coastal area) display a distinctively higher $^{143}Nd/^{144}Nd$ ratio at a given $^{87}Sr/^{86}Sr$ ratio than samples from Xilong and Longyou (inland area). Samples from Shengzhou however are separated into two groups: most samples follow the trend defined by the coastal basalts; two samples fall in the field defined by the inland basalts (Fig. 4a and Supplementary Fig. S3).

3.3. Zinc isotopes

Zinc isotopic compositions are provided in Supplementary Table S4. The $\delta^{66}Zn$ ranges from 0.30‰ to 0.45‰,

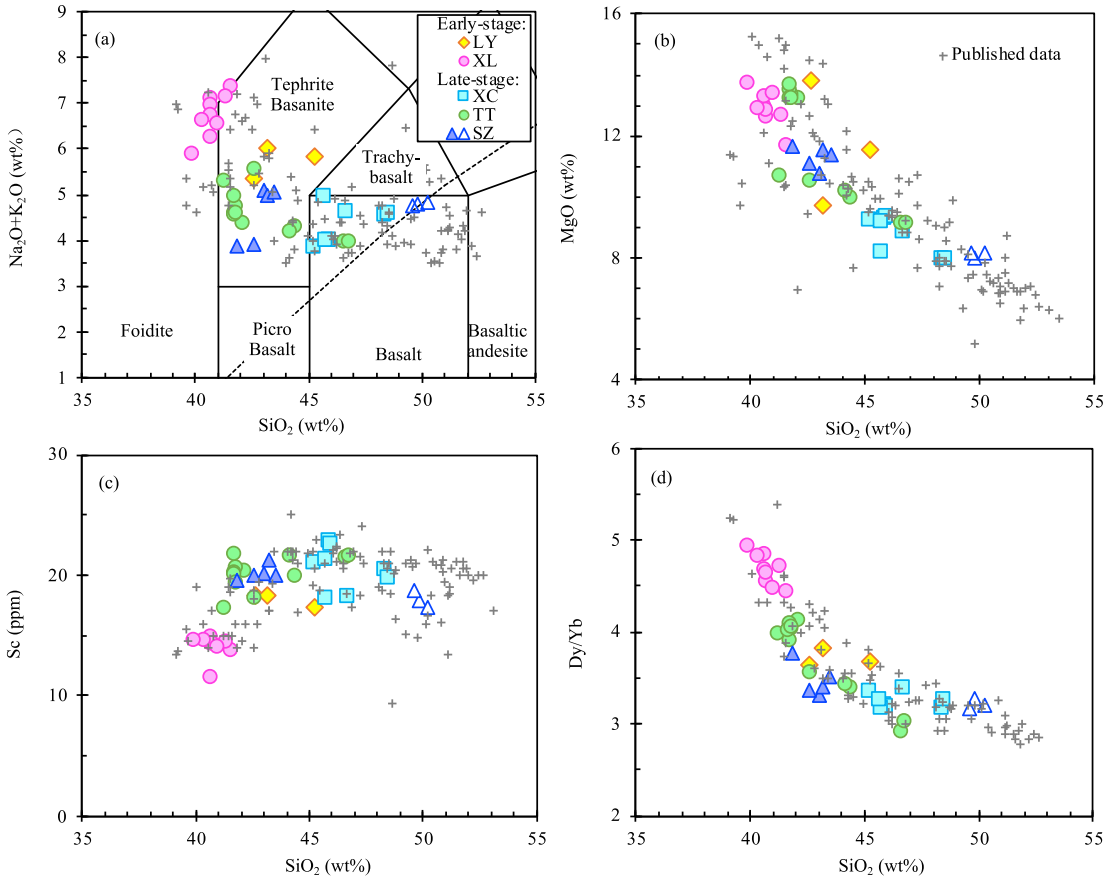

Fig. 2. (a) Total alkalis versus silica (TAS) diagram, (b) MgO versus SiO_2, (c) Sc versus SiO_2 and (d) Dy/Yb versus SiO_2 showing the compositions of the studied samples from Xilong (XL) and Longyou (LY) in the inland area, and from Xinchang (XC), Shengzhou (SZ) and Tiantai (TT) in the offshore area. Open triangles show the crustally-contaminated samples from SZ (see text for details). The grey crosses are published data for the Zhejiang basalts (see Supplementary Fig. S1 for data sources).

which is higher than of the complete range for the mantle and the oceanic crust ($\delta^{66}Zn \sim 0.2$–$0.3‰$; Wang et al., 2018). The low-silica basalts have high and a restricted range of $\delta^{66}Zn$ values (Figs. 4b, 4c, 5 and Supplementary Fig. S4). Specifically, the low-silica samples with the highest $\delta^{66}Zn$ show a moderately enriched Sr-Nd isotopic signature, contrasting with the samples with the highest $\delta^{66}Zn$ from north China reported by Wang et al., (2018) and Wang and Liu (2021) that also have the most depleted Sr-Nd isotopic signature.

In comparison to the low-silica basalts, the high-silica basalts overall show lower $\delta^{66}Zn$ values that significantly decrease with increasing SiO_2 and decreasing alkalis, Zn, Nb, Zn/Fe, La/Yb, Ba/Th and Ce/Pb (Fig. 5 and Supplementary Fig. S4).

4. DISCUSSION

4.1. Temporal-spatial-compositional variations

Because crustal assimilation can affect the original composition of the ascending magma, it is important to assess its potential role in the geochemical evolution of the selected suite of samples. Three samples from Shengzhou were likely affected by crustal contamination. These three samples are the most silica-rich (Fig. 2), have significantly higher Sr and lower Nd isotopic ratios than samples from the same locality (Fig. 4a), and have the lowest Ce/Pb and Nb/U ratios (Supplementary Fig. S5). These three samples are clearly distinct in the figures and are discarded from the discussion. The following observations suggest that the effect of crustal contamination on the other samples is negligible: (1) the samples are primitive (>8 wt. % MgO; Fig. 2). (2) Most volcanic suites (e.g., Xilong, Xinchang, Shenzhou, and Tiantai) contain abundant mantle xenoliths (Liu et al., 2012; Lu et al., 2015), indicating rapid eruption of the magma and little residence time in the crust. (3) An overall negative trend is observed in the TAS diagram (Fig. 2); significant crustal contamination would cause a positive correlation between silica and alkali contents. (4) The samples have OIB-like incompatible trace element features (e.g., negative Pb and positive Nb anomalies; Fig. 3) and their Nb/U and Ce/Pb ratios are comparable to ratios observed in MORB and OIB (Supplementary Fig. S5). Notably, the Sr-Nd isotopic ratios of early-stage low-silica basalts are similar to those of the three crustal-contaminated samples from Shenzhou. However, they are also more primitive (e.g., higher MgO) and present the highest Zn isotopic ratios (Fig. 4), in striking contrast with those affected by crustal contamination (<8 wt. % MgO and

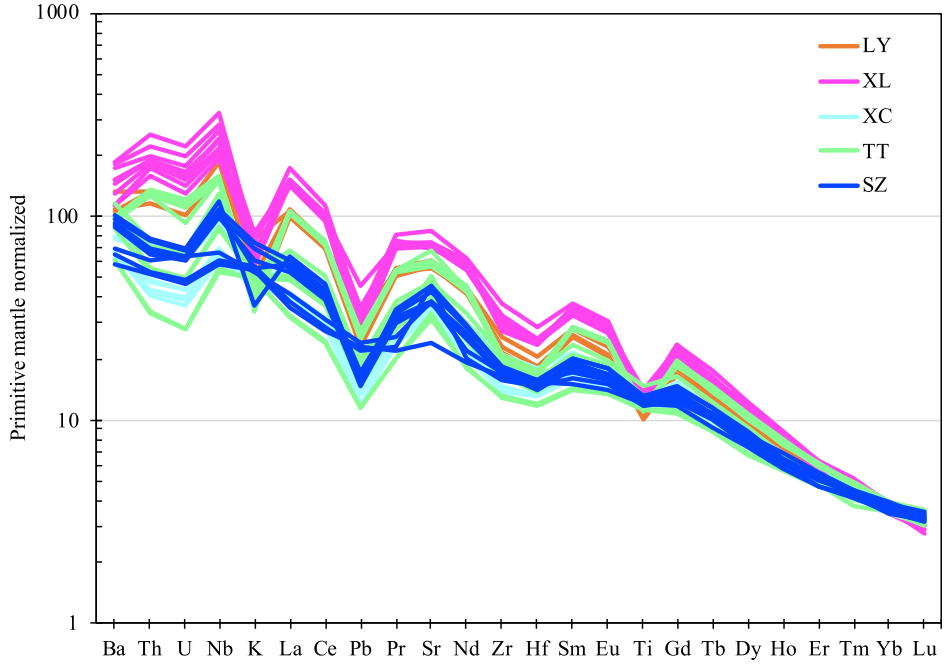

Fig. 3. Primitive mantle normalized trace element patterns for the studied samples. Primitive mantle values are from McDonough and Sun (1995).

low Zn isotopic ratios) suggesting a very different origin for the low-silica Sr-Nd isotopic signature.

Early- and later-stage magmatism shows systematic spatial and compositional differences. Compared to the late-stage basalts, the early-stage basalts have, on average, (1) higher alkali and MgO contents, lower SiO_2 and Al_2O_3 contents and higher CaO/Al_2O_3 ratios (Figs. 2 and S1), (2) higher compatible trace element contents (e.g., Ni and Cr; Supplementary Fig. S1), (3) higher incompatible trace element contents (e.g., Sr and Dy; Supplementary Fig. S1), (4) higher ratios of more to less incompatible elements (e.g., Dy/Yb; Fig. 2), (5) higher ratios of elements with similar bulk partition coefficients (e.g., Ce/Pb; Supplementary Fig. S2), (6) lower ratios of fluid-mobile to less fluid-mobile elements (e.g., K/La; Supplementary Fig. S2) and (7) higher Ni/Co, Zn/Fe and Mn/Fe ratios (Fig. 6). Finally, the early-stage basalts display a coupled Zn-Sr-Nd isotopic signal with moderately enriched Sr-Nd isotopic signatures and high $\delta^{66}Zn$, while the late-stage basalts show a decoupled signature with $\delta^{66}Zn$ decreasing with increasing SiO_2 and $^{87}Sr/^{86}Sr$ and with decreasing alkalis and $^{143}Nd/^{144}Nd$ (Figs. 4, 5). The systematic spatial, temporal, and compositional differences described here suggest that magma formation for the two groups was controlled by generally different mantle sources/processes.

4.2. Constraints on melting conditions

Yang et al. (2019) developed a parameter, FCKANTMS (see caption of Fig. 6 for its definition), to distinguish between "mafic" (bulk Mg# <85 and olivine modal abundance < 50 wt.%), "transitional", and "peridotitic" (bulk Mg# >89 and olivine modal abundance > 60 wt.%) sources using the major elements of basalts. Results plotted in Fig. 6 show that basalt compositions mostly fall in the fields of transitional and mafic lithologies. Interestingly, none of the compositions falls in the field of strictly peridotitic composition, and the good positive correlation between the Fe/Mn ratio and FCKANTMS (Fig. 6b) could suggest an increase of the mafic component towards high FCKANTMS values. However, this assumption is not supported by other transition metal concentrations. In fact, samples that show the highest Ni/Co ratios (presumably representing a peridotitic source, see Section 5.4) also present the highest Zn/Fe ratios (presumably representing an eclogitic source) (Fig. 6d; Le Roux et al., 2011). Additionally, FCKANTMS values for the early-stage basalts fall inside the range covered by the late-stage basalts. This also contrasts with our observations on the major and trace element (Fig. 2) and isotopic data (Fig. 4). Finally, comparison between basalt compositions and experimental melts (Fig. 7) shows that early-stage basalts overlap with compositions produced by reaction between carbonated eclogite melt and peridotite (Mallik and Dasgupta, 2014). The late-stage samples form a trend that extend from the most silica-deficient samples to compositions of melt produced by peridotite melting. Because of these contrasted signals, in order to determine the source lithologies involved in the generation of these basalts, it is important to characterize the melting conditions in the source.

Transitional lithologies (e.g., Lambart et al., 2009), as predicted by the FCKANTMS values, lithologies resulting from the reaction between peridotite and carbonated eclogite melt (Mallik and Dasgupta, 2014), as suggested in Fig. 7, and peridotites, all contain pyroxenes and olivine as subsolidus phases. Hence, we can use Lee et al.'s (2009) ther-

mometer and barometer to estimate the P-T conditions of melt segregation. The thermodynamic basis is the Fe-Mg exchange reaction between olivine and melt for the thermometer and the melt silica activity buffered by coexisting olivine-orthopyroxene for the barometer. In practice, the thermobarometer should only be applied to samples with SiO_2 > 40 wt.% that are simultaneously saturated in orthopyroxene and olivine in the source region, both of which are satisfied here. Moreover, the thermobarometer is suitable for melts having undergone olivine fractionation after the magma segregated from the mantle source. Except for the three SZ samples that experienced significant crustal assimilation, our samples have MgO > ~8 wt.% and SiO_2 < ~47.5 wt.%, indicating that they have primarily fractionated olivine (e.g., if significant fractionation of clinopyroxene had occurred, sensitive elements, such as Sc, would be significantly depleted in the MgO-poor and SiO_2-rich samples, which is not observed). For fO_2 in the calculations, we assume a magmatic $Fe^{3+}/\Sigma Fe$ of 0.15. In fact, recent olivine-melt partitioning measurements for V suggest that Cenozoic basalts in eastern China have a high fO_2 due to recycling of carbonate (Hong et al., 2020). This is consistent with the V/Sc ratios of the basalts that fall into the field of OIBs (Supplementary Fig. S6) that are, overall, slightly more oxidized than MORB (Moussallam et al., 2019). For magmatic H_2O contents, we use the average of 2.0 wt.% obtained from clinopyroxene FTIR data (Liu et al., 2016b). For olivine Fo content in the mantle source, we assume Fo_{90}, which is close to that of the DMM (Workman and Hart, 2005). Although there must be natural variation of olivine Fo content in the mantle source, a ± 1 variation in Fo value will propagate to P-T estimates generally within the uncertainty of Lee et al's thermobarometer. Furthermore, considering our samples have a hybrid source, Fo_{90} should be regarded as a maximum value. Prescribing a lower Fo content will shift the estimation to lower P-T conditions, and therefore the P-T obtained here should be considered as maximum values.

With the above constraints, calculations using Lee et al. (2009) thermobarometer reveal that two groups of samples with distinct trends can be identified on a SiO_2 vs. pressure diagram (Supplementary Fig. S7). Early-stage basalts display relatively high calculated pressures, low SiO_2 contents (< ~43 wt.%) and small variations of the silica content; on average, the late-stage basalts exhibit lower pressures, and both higher concentrations and larger variations in silica (blue line in Supplementary Fig. S7). We attribute this phenomenon to the presence of CO_2 in basalts with SiO_2 < ~43 wt.% (see Section 4.3). Lee et al. (2009) empirical model does not take into account the impact of CO_2 on the silica activity. Therefore, applying these thermobarometers to carbonated melts can result in large uncertainties on P-T estimates. Hence, we employ an additional step here to

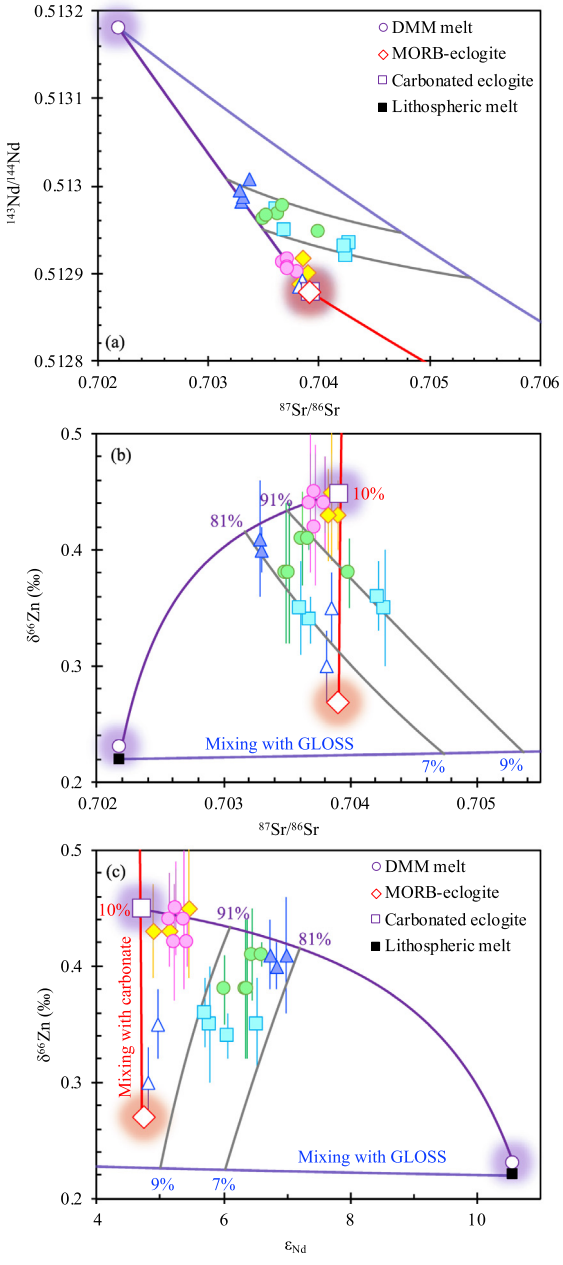

Fig. 4. (a) Variation of $^{143}Nd/^{144}Nd$ versus $^{87}Sr/^{86}Sr$ for the studied basalts. Error bars (2σ) are smaller than the symbols. (b-c) Variation of $\delta^{66}Zn$ as a function of $^{87}Sr/^{86}Sr$ and ε_{Nd} for the studied basalts. Error bars represent 2σ. Also shown for comparison are the isotopic compositions of DMM, MORB-eclogite (altered oceanic crust), carbonated eclogite, lithospheric mantle melt and GLOSS (mean composition for subducted sediments). The red line illustrates mixing between MORB-like eclogite and carbonate components to form the carbonated eclogite component. The purple curve represents the mixing line between DMM and carbonated eclogite components. The blue line represents mixing between the lithospheric mantle and GLOSS components and the gray lines illustrate the mixing range between the asthenospheric components and the subduction modified lithospheric component. Choices of Zn-Sr-Nd isotopic compositions and element contents of the modeled endmembers and the details of the isotopic calculations are provided in Supplementary Text S3. Symbols for the studied samples are the same as in Fig. 2. See also Supplementary Fig. S9 for an enlargement of Fig. 4a and the full range of Fig. 4b that shows all the end members including GLOSS and carbonate sediments.

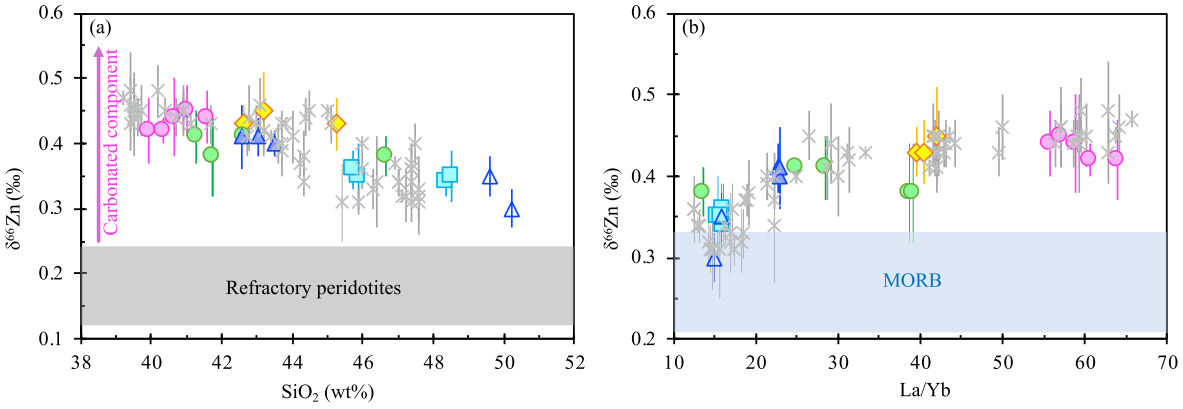

Fig. 5. Variations of $\delta^{66}Zn$ with (a) SiO_2 and (b) La/Yb. Data for alkali basalts from Shandong, North China craton (grey cross symbols) are from Wang et al. (2018). Data source for $\delta^{66}Zn$ of refractory peridotites is in Wang et al. (2018). The pink arrow indicates increasing contribution from the carbonated component. Symbols are the same as in Fig. 2. (See Supplementary Fig. S4 for variations with total alkali, Zn and Nb contents and with Zn/Fe, Ba/Th and Ce/Pb ratio).

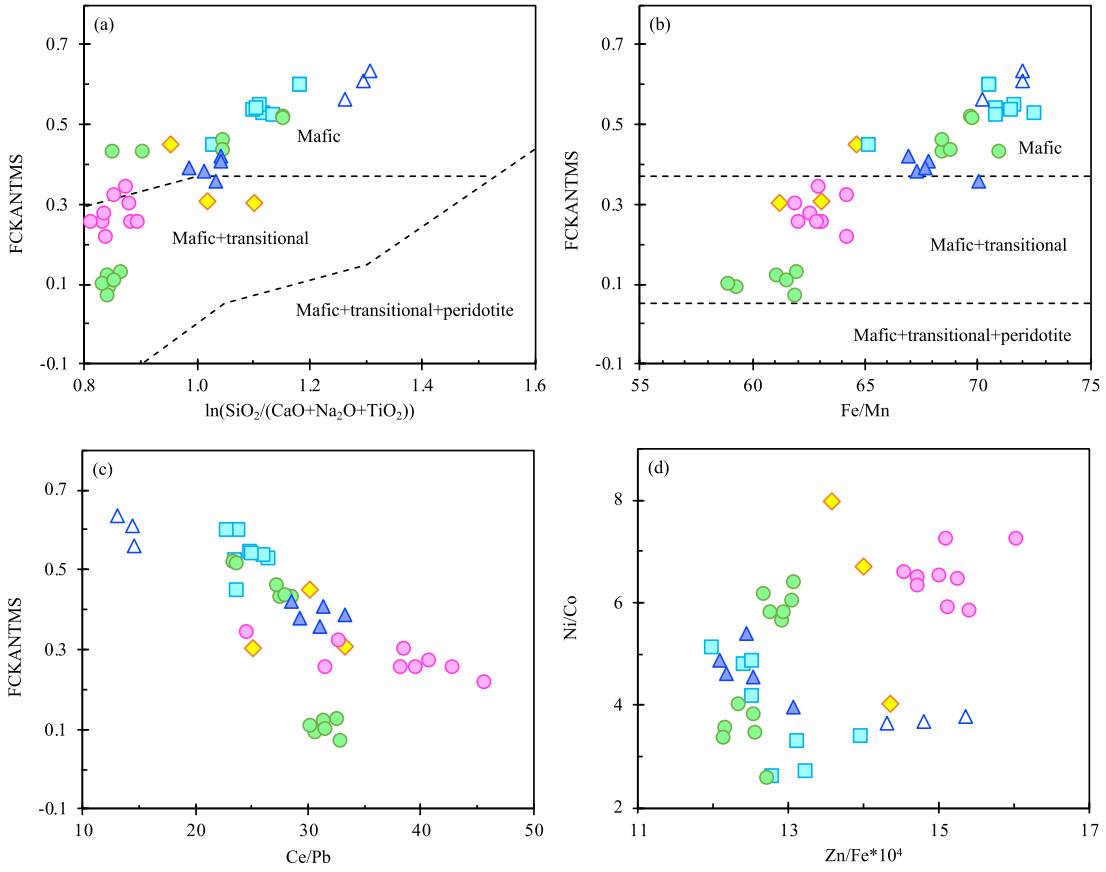

Fig. 6. (a-c) FCKANTMS (FCKANTMS = $\ln(FeO/CaO) - 0.08*\ln(K_2O/Al_2O_3) - 0.052*\ln(TiO_2/Na_2O) - 0.036*\ln(Na_2O/K_2O)*\ln(Na_2O/TiO_2) - 0.062*(\ln(MgO/SiO_2))^3 - 0.641*(\ln(MgO/SiO_2))^2 - 1.871*\ln(MgO/SiO_2) - 1.473$, in wt.%) as function of (a) $\ln(SiO_2/(CaO + Na_2O + TiO_2))$, (b) the Fe/Mn ratios, and (c) the Ce/Pb ratios for the studied basalts. Dashed lines in (a) and (b) indicate the boundaries between the various lithologies potentially present in the magma source defined by Yang et al. (2019). (d) Ni/Co ratios as function of the $Zn/Fe*10^4$ ratios in the studied basalts. Symbols are the same as in Fig. 2.

correct the effect of CO_2 on P-T estimation for basalts with $SiO_2 < \sim 43$ wt.% (See Supplementary Text S2 for details on the applied correction).

After P-T correction, we find that our samples equilibrated with or segregated from the mantle source between ~ 1380–1515 °C and ~ 2.2–4.0 GPa (Fig. 8). The

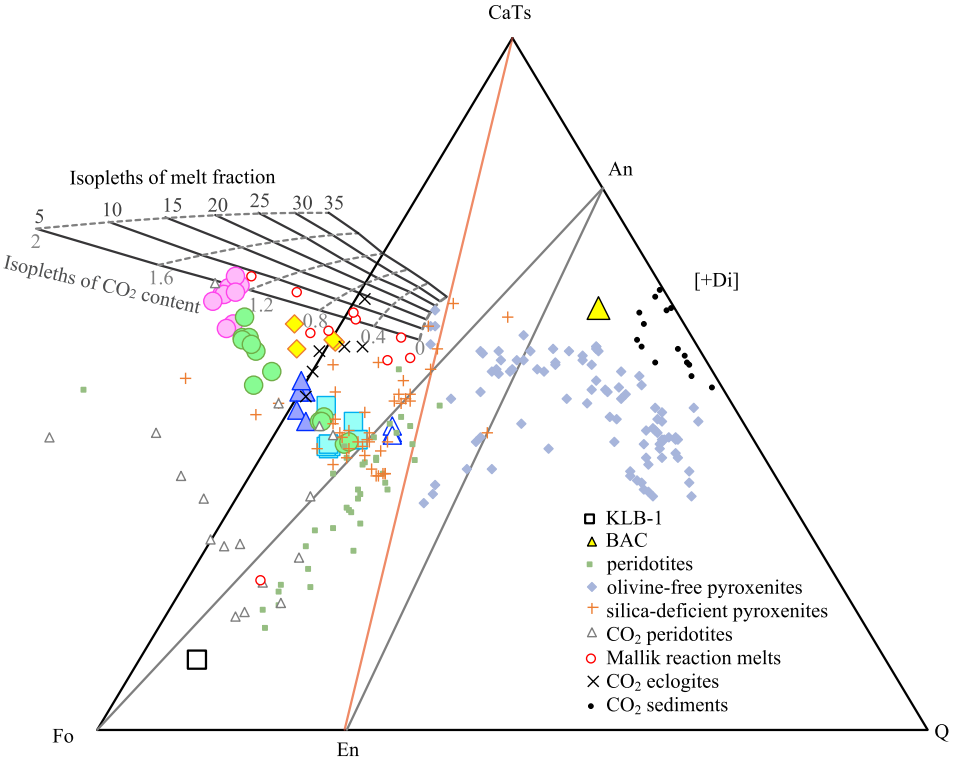

Fig. 7. The studied basalts compared to experimentally derived partial melt compositions of dry peridotite (Takahashi and Kushiro, 1983; Takahashi and Scarfe, 1985; Takahashi et al., 1993; Walter, 1998), MORB-eclogite (Pertermann and Hirschmann, 2003; Spandler et al., 2008), silica-deficient pyroxenite (Hirschmann et al., 2003; Keshav et al., 2004; Kogiso and Hirschmann, 2006; Lambart et al., 2013), carbonated eclogite (Dasgupta et al., 2006; Gerbode and Dasgupta, 2010), carbonated peridotite (Hirose, 1997; Dasgupta et al., 2007) and carbonated sediment (Tsuno and Dasgupta, 2011) on the Ca-Tschermak-Anorthite-Quartz-Enstatite-Forsterite (CaTs-An-Q-En-Fo) plane from Diopside (Di), after the projection scheme of O'Hara (1968). The CaTs-En join is a thermal divide composed of garnet-pyroxene. Also shown are volatile-free peridotite (KLB-1), experimental basaltic andesite composition (BAC; Mallik and Dasgupta, 2012) and modelled isopleths of melt compositions from MORB-eclogite melt-peridotite reaction (Mallik and Dasgupta, 2014). The solid and dashed lines with numbers represent eclogite melt fraction (5–35%) and amount of CO_2 (0–2%) in the source, respectively.

majority of P-T data plots close to the 1420 °C mantle adiabat, which is slightly higher than the upper end of the global variation of normal mantle potential temperature (Tp ~ 1350–1410 °C). Considering small amounts of carbonated eclogite were involved in mantle melting (see Section 4.3), the melting temperature obtained here can only be considered as a maximum value. These temperatures are not consistent with the significant positive thermal anomaly usually required for deep-rooted hot spots (Herzberg et al., 2007). The absence of deep-rooted mantle plume is also consistent with seismic results in this region (Huang and Zhao, 2006). All these imply that, consistent with previous studies (Li et al., 2015; Liu et al., 2016b; Sun et al., 2017; Jin et al., 2020), our samples were most likely generated by adiabatic decompression melting of the asthenosphere containing variable amounts of $H_2O \pm CO_2$, rather than an active upwelling mantle plume.

Remarkably, while most of the early-stage samples plot at asthenospheric T and P, later-stage magmatism extends into the base of the sub-continental lithospheric mantle (SCLM), corresponding to the depth of lithosphere-asthenosphere boundary (LAB, ~80–100 km) (Ma and Wu, 1987; Chung et al., 1994; Sun et al., 2017). The later-stage magmas also plot close or slightly below the 1420 °C adiabat, that is at P-T conditions significantly hotter than the expected conditions for the cold lithospheric mantle. This suggests that either they represent adiabatic melting/melt ascending path or they did not significantly re-equilibrate with the conditions of the lithospheric conductive geotherm. These observations suggest that both the carbonated asthenosphere and lower part of the lithospheric mantle were involved in magma genesis, as we will discuss later.

4.3. Early-stage low-silica samples: melts of carbonated eclogite-bearing asthenosphere

As discussed in Section 4.2, major element data suggest melting of a peridotitic mantle alone cannot account for the genesis of our low-silica basalts and a lithologically-heterogeneous mantle source should be involved. This is further supported by the observation that peridotites intensively metasomatized by carbonatites or carbonated silicate melts seem to still preserve mantle-like Mg isotopic compo-

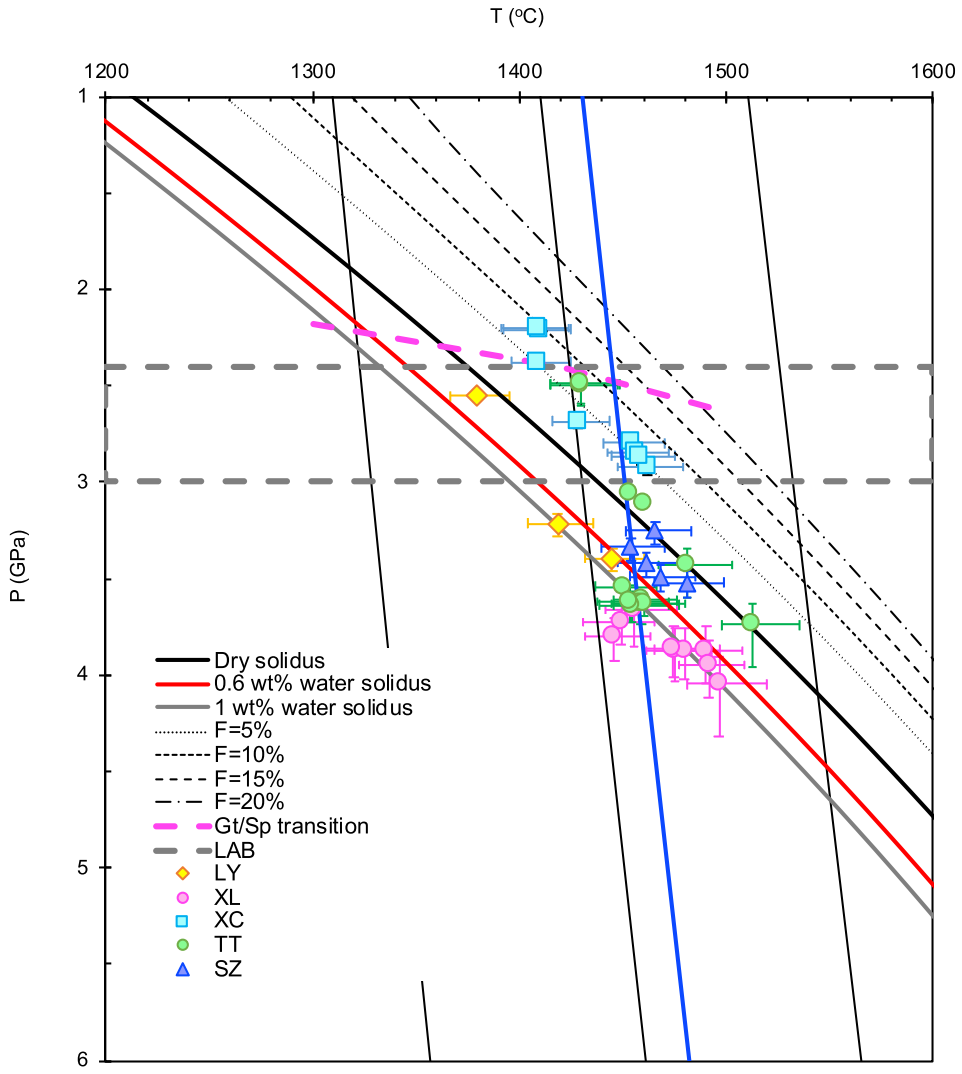

Fig. 8. Melting P-T conditions for the studied basalts. Source for the anhydrous peridotite solidus and the hydrous peridotite solidus with 0.6 wt.% and 1.0 wt.% H_2O and the detailed calculations of melt fraction lines with F = 5, 10, 15 and 20% can be found in Fig. 7 of Xu et al. (2020a). Near vertical lines are mantle adiabats with potential temperature of 1300, 1400, 1500 and 1600 °C (black) and ~ 1420 °C (blue), respectively. LAB denotes lithosphere-asthenosphere boundary. Data source for the garnet/spinel (Gt/Sp) transition is from Klemme and O'Neill (2000). Symbols are the same as in Fig. 2. The three samples affected by crustal contamination are not plotted.

sitions (-0.27‰ to − 0.10‰) (Wang et al., 2016), and clearly cannot account for the low-δ^{26}Mg (-0.46 ± 0.14‰) of the low-silica basalts (Huang et al., 2015; Li et al., 2016; Jin et al., 2020). Therefore, at least one additional component originating from the asthenosphere has played an important role in the low-silica melt formation.

Trace element characteristics of the early-stage samples show pronounced peaks (i.e., relative enrichments) for elements, such as Nb, LREEs and Sr, and negative anomalies (relative depletions) for elements, such as K, Pb, Zr, Hf and Ti (Fig. 3), resulting in high Ce/Pb, low K/La and Ti/Eu ratios, similar to trace elements patterns in rocks with high U/Pb (or high mu - HIMU) ratios. Rocks with HIMU type trace element and isotopic compositions, e.g. unradiogenic $^{87}Sr/^{86}Sr$ (<0.7040) and intermediate $^{143}Nd/^{144}Nd$ (~0.5128–29), are commonly interpreted to be derived from a source containing recycled dehydrated oceanic crust (MORB-like eclogite) (Hofmann, 1997). However, the pronounced negative anomalies for high field strength elements Zr, Hf and Ti in early-stage samples (Fig. 3) are similar to those observed in oceanic carbonatites (Hoernle et al., 2002), some ocean island basalts (Castillo, 2015) and continental intraplate basalts (Zeng et al., 2010). Partitioning reaction between low-silica, CO_2-rich melts and carbonated eclogite may account for such Zr-Hf-Ti depletions, high alkali contents, elevated CaO/Al_2O_3 and low Ti/Eu ratios of these low-silica samples.

Because of the remarkable compositional difference between silicates and carbonates (Liu and Li, 2019 and references therein), zinc isotopic ratios have proven to be a very efficient tool to identify the involvement of recycled carbonates in magmatic processes (Liu et al., 2016a, 2020;

Wang et al., 2018; Beunon et al., 2020; Jin et al., 2020; Kong et al., 2022; Li et al., 2021; Wang and Liu, 2021). Zinc isotopic compositions of the Zhejiang basalts ($\delta^{66}Zn$ = 0.30‰–0.45‰) extend well beyond the field of peridotitic mantle (Doucet et al., 2016; Wang et al., 2017; Huang et al., 2018a, 2019; Sossi et al., 2018; Liu and Li, 2019; Doucet et al., 2020) and MORB ($\delta^{66}Zn < \sim$0.30‰) (Wang et al., 2017; Huang et al., 2018b; Liao et al., 2020) and cannot be explained by melting, crustal contamination or fractionation processes. In fact, for the range of MgO contents observed in our samples (7.9–13.8 wt.%), crustal assimilation and/or fractionation of olivine and clinopyroxene during magma ascent can only produce small Zn isotope fractionation (less than 0.1‰) (Chen et al., 2013; McCoy-West et al., 2018; Yang and Liu, 2019). Similarly, Zn isotope fractionation during partial melting rarely exceeds ~ 0.1‰, (Wang et al., 2017). In addition, Cr-spinel/chromite fractionation during magma evolution will lead to higher $\delta^{66}Zn$ but lower Zn contents than the unfractionated primary magma (Yang et al., 2021a), which is in contrast with our samples that show both high $\delta^{66}Zn$ and Zn contents. Therefore, the Zn isotopic compositions of our basalts most likely reflect their mantle source characteristics.

Slab dehydration in subduction zones liberates hydrous fluids with high $\delta^{66}Zn$ (Pons et al., 2016), and the residue, a dehydrated MORB-eclogite, should therefore (due to mass balance) possess lower $\delta^{66}Zn$ than a MORB protolith. A dehydrated MORB-eclogite therefore cannot be responsible for the high $\delta^{66}Zn$ of our samples. Hence, combining high $\delta^{66}Zn$ values and carbonate-imprinted major and trace element signatures (see above), we consider that recycled carbonated eclogite is the most likely candidate for the high-$\delta^{66}Zn$ agent. This conclusion is also supported by the observation that our low-silica samples have CaO/Al_2O_3 ratios (0.71–0.98) and TiO_2 contents (2.02–2.80 wt.%) within the range of experimental partial melts of carbonated silica-excess eclogite (CaO/Al_2O_3 = 0.5–1.0 and TiO_2 = 1.9–3.9 wt.%) (Gerbode and Dasgupta, 2010), consistent with the involvement of a carbonated MORB-like eclogite source. We note that melting of carbonated sediments could also produce high $\delta^{66}Zn$, but would also result in elevated K contents and K/Na ratios (Tsuno and Dasgupta, 2011), not consistent with our major element observations (Supplementary Table S1; Fig. 7). Finally, although it is impossible to completely rule out the possibility that the source of carbon is an ancient isolated primordial mantle reservoir, the lack of experimental data does not allow us to predict if low-degree incipient carbonatite melts originating from such a pristine carbon-bearing source are capable of having high-$\delta^{66}Zn$ values compatible with those of natural basalts.

Following the method of Beunon et al. (2020), calculations using a simple mixing model (see details in Supplementary Text S3) reveal that mixing of ~ 10% carbonates with MORB-eclogite can reproduce carbonated eclogite melt with $\delta^{66}Zn$ as high as 0.45‰ (Fig. 4b-c). Subsequent blending of this high-$\delta^{66}Zn$ carbonated eclogite component with less than 5% matrix DMM-derived low-degree melt (F = 1%) would generate both the elevated Zn isotopic ratios and the relatively enriched Sr-Nd isotopic compositions of the low-silica samples (Fig. 4), which explains their coupled Zn-Sr-Nd isotopic signatures. We acknowledge that the results are model-dependent and using other end-member compositions will change the proportion of each end-member in the mixing calculations. However, estimating the absolute proportions of each end-member is beyond the scope of this study. Our goal is to demonstrate that we can reproduce the geochemical trends, and especially the coupled versus decoupled Zn-Sr-Nd isotopic signatures of these two groups of basalt using our mixing model. This model also explains the good correlations between melting depth proxies (e.g., SiO_2 and Dy/Yb), melting degree-sensitive element ratios (e.g., La/Yb) and the source-variation-sensitive ratios (e.g., Ti/Eu and Ba/Th; Fig. 9), highlighting that the high-$\delta^{66}Zn$, and low Ti/Eu, Sr/Nd, K/La and Ba/Th signature of the fusible carbonated eclogite can only be preserved in high pressure, low degree melts. The P-T equilibrium constraints provide further support that the low-silica melts come from a deep source (Fig. 8). We note that one of the early-stage basalt (18LY02) plots at a significantly lower P and T, in the range of the lithosphere-asthenosphere boundary (LAB). This sample has high $\delta^{66}Zn$ (Fig. 4) coupled with high La/Yb and Dy/Yb, and low Lu/Hf, Ti/Eu, K/La and Ba/Th ratios, similar to other early-stage samples (Fig. 9). Hence this sample was most likely also generated in the asthenosphere, and then its major element composition was equilibrated at the LAB during magma ascent.

A carbonated eclogite-bearing asthenospheric source for low-silica samples has also been proposed by Wang et al. (2018) for basalts from Shandong (North China Craton). However, in this area, the low-silica samples show strongly decoupled Zn-Sr-Nd signature (the samples with the highest $\delta^{66}Zn$ are also the samples with the most depleted Sr-Nd isotopic signatures; see Fig. 2H and Fig. DR5 in Wang et al., 2018), which contrasts with our observations (Fig. 4). Our low-silica samples with the highest Zn isotope ratios show moderately enriched Sr-Nd isotopic signature, highlighting that the coupled enriched Zn-Sr-Nd isotopic signal of the carbonated eclogite component can only be preserved by low degree partial melts. This is further supported by the fact that the low-silica samples from Xilong have the highest incompatible element contents (e.g., Nb content up to ~ 300 ppm) and hence likely represent the lowest melting degrees among all of the Cenozoic basalts in eastern China reported so far (see compilation in Xu et al., 2020b).

4.4. Later-stage high-silica samples: products of carbonated asthenosphere-lithosphere interaction

Although there is a consensus that partial melting of a heterogeneous asthenosphere contributes to the geochemical variation of the early-stage mafic volcanic rocks (Ho et al., 2003; Li et al., 2015; Liu et al., 2016b; Sun et al., 2017; Jin et al., 2020), the origin of the late-stage high-silica group samples remains contentious. Some studies favored the involvement of a silica-rich component in the asthenosphere (Li et al., 2015; Liu et al., 2016b; Jin et al., 2020), whereas others suggested that the lithospheric man-

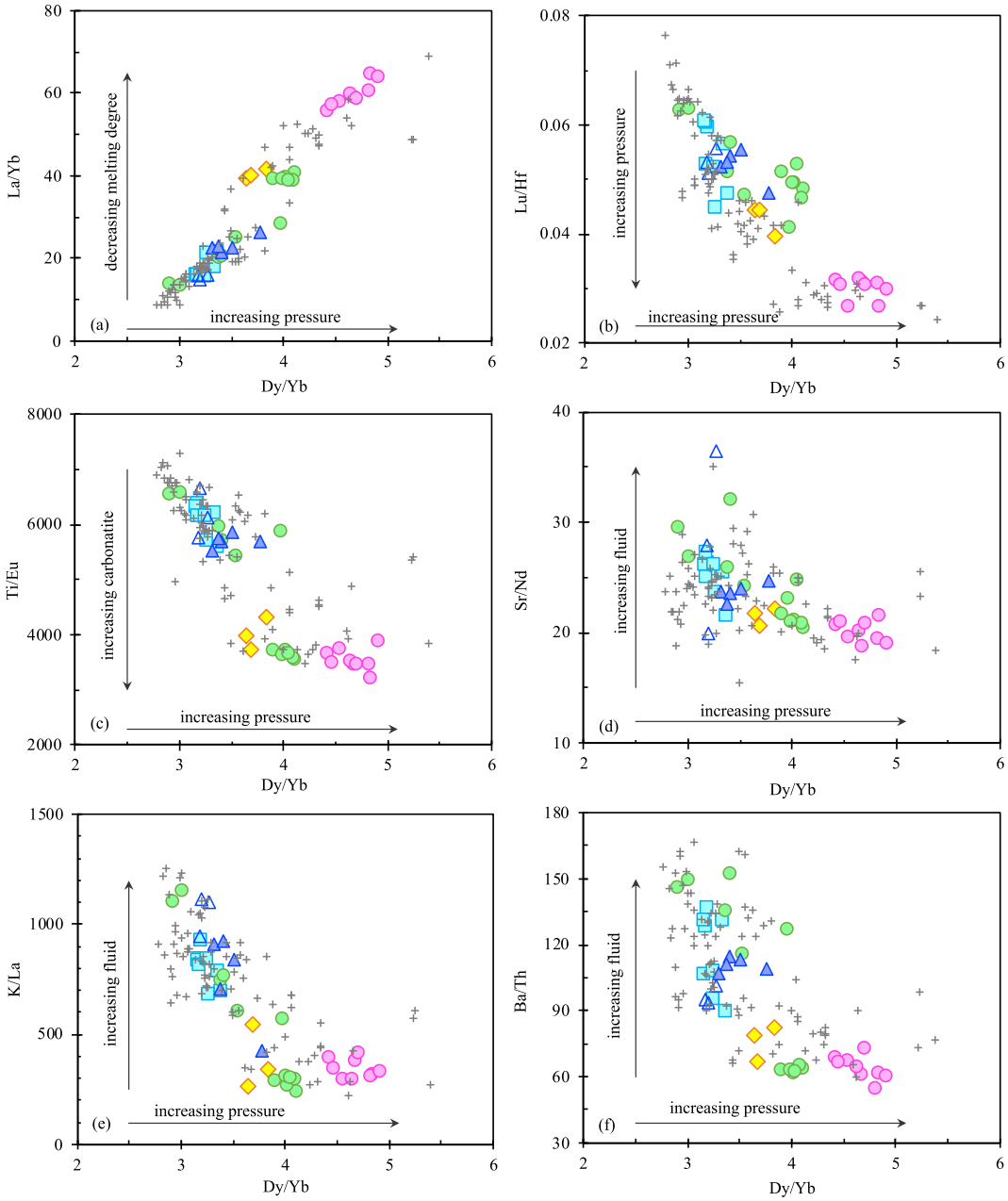

Fig. 9. La/Yb, Lu/Hf, Ti/Eu, Sr/Nd, K/La, Ba/Th versus Dy/Yb for the studied basalts. Horizontal arrows indicate increasing melting pressure in (a-f). Vertical arrows indicate decreasing melting degree in (a), increasing melting pressure in (b), increasing contribution from carbonatite melt in (c) and increasing contribution from subduction-modified sub-continental lithospheric mantle in (d-f). Symbols are the same as in Fig. 2.

tle could play a role in the geochemical variation of the magmas, by either acting as a rigid lid that limits the final depth of melting and/or by directly contributing to the melt (Ho et al., 2003; Sun et al., 2017). Albeit our P-T estimates show that melt equilibration depths for the high-silica group range from the asthenospheric mantle to the lithosphere-asthenosphere boundary (~80–100 km) (Ma and Wu, 1987; An and Shi, 2006), the unique P-T condition represented by each basalt may, however, not necessarily reflect a melting process. Two possible scenarios exist: in the first case, the melt thermobarometer only records the final P-T of melt equilibration (i.e., the P-T conditions of melt segregation); in the second case, the thermobarometer records the average P-T conditions of the melting column. In the first case, the shallowest P-T estimate could be explained by melt-rock reactions in the SCLM during magma transport. In the second case, direct melting of the lower part of the SCLM must be involved. Addition-

ally, samples may have been re-equilibrated at shallower conditions during magma transport (as suggested for 18LY02). However, this would result in a significantly lower temperature as the re-equilibrated sample would plot closer to the lithospheric geothermal gradient. This is not observed in the late-stage samples. P-T calculations also reveal that high-silica group melt generation also occurred in the garnet peridotite stability field (Fig. 8), which is further supported by the low Lu/Hf (<0.07) and high Dy/Yb ratios (>2.9) observed in all samples (Fig. 9). [For comparison, the average N-MORB has Lu/Hf ~ 2 and Dy/Yb ~ 1.7 (Gale et al., 2013)]. The negative correlation between Lu/Hf and Dy/Yb ratios suggests a decrease of the residual garnet mode from the low-silica group to the high silica group that also supports shallower melting depths for the high-silica samples.

In Section 4.3, we identified two components to explain the early-stage magmatism: DMM and a carbonated eclogite derived from a previously subducted slab containing both eclogite and carbonate. Fig. 4a shows that at least a third component is required to account for the Sr-Nd isotopic variations of the high-silica group. This third component is characterized by more radiogenic Sr and less radiogenic Nd isotopic ratios, but by a lower δ^{66}Zn compared to the isotopic composition of the carbonated eclogite. It was recently proposed to be recycled Pacific oceanic crust in the form of eclogite/pyroxenite (Li et al., 2015; Liu et al., 2016b; Jin et al., 2020). In fact, higher values for the FCKANTMS parameter (Yang et al., 2019) and lower Ni/Co ratios (Le Roux et al., 2011) may suggest a higher proportion of a mafic component. However, this is not consistent with the relatively low Zn/Fe ratios observed in the high-silica group that suggest a peridotitic source (Fig. 6 and Supplementary Fig. S4c). Additionally, FCKANTMS values for the late-stage basalts are not systematically higher than the values for the early-stage basalts, but also expand toward slightly lower values. We propose that the third component could be the subduction-modified SCLM. Although no whole rock trace element data have been reported for the peridotite xenoliths in the Zhejiang area, available trace element data for Cpx in peridotite xenoliths from the SCLM beneath the Zhejiang area show enrichment in fluid-mobile trace elements such as U, Pb and Sr in the primitive mantle-normalized trace element diagram (Liu et al., 2012; Lu et al., 2015). In addition, whole rock trace element data of peridotite xenoliths in the adjacent Lianshan area also display enrichment in fluid-mobile trace elements (Lu et al., 2013). Finally, arc-like trace element features (e.g., LILE enrichment and HFSE depletion) and enriched Sr-Nd isotopes are also recorded in the SCLM-derived lavas, indicating the SCLM under South China have been modified by subducted sediment-derived melt during the Mesozoic Paleo-Pacific Plate subduction (Guo et al., 2021; Wang and Yan, 2021). All these support the presence of subduction-modified SCLM at depth. A contribution of melts derived from an overlying, metasomatized refractory harzburgitic lithosphere in the formation of later stage basalts can explain 1) their relatively low Dy/Yb and high Lu/Hf ratios (Fig. 9), consistent with the thermobarometer constraints (Fig. 8), 2) their major element compositions that suggest an increase of the contribution of peridotite melt (Fig. 7), 3) their high K/La, Ba/Th and Sr/Nd (Fig. 9), indicating a greater contribution from subduction-modified SCLM components (McGee et al., 2013), 4) their enriched Sr-Nd isotopic compositions that are similar to those reported for peridotite xenoliths found in alkali lavas (Supplementary Fig. S3), and 5) their low Ni/Co ratio. In fact, Co being less compatible than Ni in olivine (Herzberg et al., 2016) and a higher proportion of the olivine in the source, as expected in a residual lithology, should result in a lower Ni/Co ratio in the melt. In addition, Ni and Co concentrations in basalts, both from early and late-stage magmatism, can be explained by fractionation of olivine from a peridotite melt (Supplementary Fig. S8).

Isotopic modelling shows that mixing of 7–9% subducted sediment with partial melts of SCLM could well account for the enriched Zn-Sr-Nd isotopic compositions of the high-silica samples (Fig. 4). Further evidence in support of the involvement of subduction-related lithospheric mantle in the magma genesis comes from lead isotopes: high-silica basalts in North China show strong EM1 signature, while those in South China contain EM2-type enriched component. Considering that large-scale convection of asthenosphere tends to remix any zonation of geochemical heterogeneities, it is more likely that the zonation of the EM1 and EM2 component is stored in the SCLM (e.g., Xu et al., 2018; Zou et al., 2000). Although mantle xenoliths in SE China have generally depleted Sr-Nd-Pb isotopic compositions, some xenoliths present compositions pointing toward the EM2 endmember. This signature was interpreted as introduced in the SCLM by the Mesozoic Pacific plate subduction activities (Tatsumoto et al., 1992). Hence, the EM2 signature of basalts from South China also supports sediment-derived fluid incorporated in the lower SCLM during subduction episodes. This isotopically enriched SCLM component was later sampled, via either direct lithospheric melting or carbonated melt-lithosphere reaction, by the Cenozoic asthenospheric-derived melts.

Melting of a subcontinental harzburgite might also explain the higher Fe/Mn ratios and FCKANTMS values observed in some of the late-stage basalts (Fig. 6b). In fact, because iron is more compatible than Mn in olivine, the residual mantle is expected to be richer in iron and poorer in Mn than the asthenospheric mantle (e.g., Lee, 2004). Additionally, partial melting of residual harzburgite is known to produce silica-rich melt in comparison to lherzolite melting (e.g., Falloon and Danyushevsky, 2000). Finally, many lithospheric mantle samples are known to be richer in SiO_2 and contain a higher proportion of orthopyroxene than the expected residual mantle from partial melting (e.g., Kelemen et al., 1992). All these factors will result in an increase of the Fe/Mn ratio and silica content of the melt.

There are some major flaws in the model of a carbonated melt reacting with a refractory lithosphere to produce the high-silica basalts, as this implies a pure melt-rock reaction without melting, which may not act as a viable mechanism to account for the origin of high-silica alkali basalts. First,

interaction between carbonated silica-undersaturated melt and lithospheric peridotite would preferentially precipitate olivine and clinopyroxene at the expense of orthopyroxene (Wyllie and Huang, 1976; Zhang et al., 2017; Aulbach et al., 2020), through the reaction:

$$3Mg_2Si_2O_6\ (Opx) + CaMg(CO_3)_2\ (melt) = CaMgSi_2O_6\ (Cpx) + 3Mg_2SiO_4\ (Ol) + SiO_2\ (melt) + 2CO_2\ (melt).$$

Due to Opx dissolution and Ol + Cpx crystallization, an increase of SiO_2 and decrease of MgO, Ni, Cr and Sc in the reacted melt is expected. Although this is consistent with the higher SiO_2 and lower MgO, Ni and Cr content of high-silica samples compared to the low-silica basalts, the positive correlation between SiO_2 and Sc (Fig. 2c) for the primitive samples argues against this expectation. Second, large variations of Dy/Yb and Ti/Eu ratios (Fig. 9) cannot be caused by a reaction process involving only Ol, Cpx and Opx; these minerals do not significantly fractionate Dy and Ti from Yb and Eu, respectively (e.g., Halliday et al., 1995 and references therein). Third, while alkali contents are lower in high-silica basalts than in low-silica basalts (Fig. 2), the reaction of a melt with a subsolidus lithospheric mantle should result in melt consumption (Lambart et al., 2012) and increase of the incompatible element concentration, such as Na and K, in the residual melt. Finally, because Zn content of orthopyroxene is too low, the reactive process cannot produce $\delta^{66}Zn$ as low as observed in the high-silica samples (Wang et al., 2018). Therefore, the generation of the high-silica samples most likely involve partial melting of the lower sub-continental lithospheric mantle. Although it seems petrologically difficult to remelt a refractory harzburgitic lithosphere due to its relatively high solidus temperature, we propose that such melting scenario can be achieved if the following two requirements are met: (1) the SCLM is not a simple melting residue but has been metasomatized during later subduction and (2) infiltration of asthenospheric-derived volatile-rich (e.g., high CO_2 and H_2O concentrations) low-silica melt into the overlying lithospheric mantle can induce flux melting of the subduction-modified SCLM. The former criteria is supported by recent geochemical studies of Cretaceous arc-like rocks in South China that show that these magmas are formed in an active continental arc and that their SCLM source has been metasomatized by melts/fluids from subducted sediment (Guo et al., 2021). The latter condition is supported by the high water (up to 2.6 wt.%; Liu et al., 2016b) and high CO_2 contents (2.4–5.5 wt.%; calculated using the simple model of Dasgupta et al., 2013) estimated for the asthenospheric derived low-silica melt from Zhejiang. We also want to highlight that the overall depleted isotopic compositions of mantle xenoliths in SE China (Tatsumoto et al., 1992; Qi et al., 1995) cannot be used as evidence against the contribution of the SCLM, because these shallow-seated, isotopically depleted xenoliths do not often have a cogenetic relationship with the host basalts with a deeper origin. The above discussion indicates that melting of the fluid-mobile incompatible trace element and Sr-Nd isotopically enriched SCLM to produce the late-stage high-silica basalts is highly likely.

The high-silica alkali basalts thus offer an opportunity to elucidate the processes involved during melt-lithosphere interactions. Our study allows us to define three components directly participating to magma genesis: one pure component represented by the ubiquitous depleted asthenospheric peridotite (i.e., DMM), and two mixed components: a carbonated eclogite produced by mixing between recycled MORB-type eclogite and carbonate, and a refractory harzburgitic SCLM, metasomatized by subducting sediments during fossil subduction. The relative contributions of these discrete components to the final erupted melts are controlled by melting conditions (i.e., pressure and degree of melting) and time, which should be self-consistent within a geodynamic context.

To further constrain the relative contributions of the subduction-modified lithospheric mantle and of the carbonated eclogite-bearing asthenosphere, we constructed a simple melt mixing model using Zn and Sr-Nd isotopic ratios (Figs. 4 and S9). Zn-Sr-Nd isotopic compositions and element contents of the modeled endmembers and details of the isotopic calculations are provided in Supplementary Text S3. Our model predicts the depleted endmember of the late-stage basalts can be produced by mixing of ~ 9–19% depleted peridotite mantle-derived melt with carbonated eclogite melt (~81–91%) (Fig. 4) at asthenospheric pressures (Fig. 8). During subsequent mantle decompression, the depleted late-stage basalts samples mix with melt derived from the subduction-modified lithospheric mantle, resulting in an increase of the Sr isotopic ratio and a decrease of the Nd and Zn isotopic ratios. While the XC samples show the strongest lithospheric signature (i.e., the most decoupled Zn-Sr-Nd isotopic signature and the highest FCKANTMS values), the increase of the lithospheric component contribution is best illustrated by the TT samples. A slightly higher degree of melting and a limited contribution of the SCLM can explain the lowest FCKANTMS values (Fig. 6) and the highest P of melting of the late-stage basalts (Fig. 8), as well as the slightly more depleted isotopic signal in comparison to the inland basalts (Fig. 4). As decompression continues, TT samples record a higher contribution of the SCLM that dilutes the asthenospheric signal. Mixing of carbonated asthenospheric melt with melt derived from a metasomatized lithosphere also explains the correlations between alkalis, SiO_2, Nb contents, La/Yb, Ba/Th and Ce/Pb ratios and Zn isotopes for the high-silica samples (Fig. 5 and Supplementary Fig. S4), and consequently may elucidate the origin of the decoupled Zn-Sr-Nd isotopic signal of both the later-stage samples and other continental intraplate basalts.

4.5. Small-scale convection as possible geodynamic trigger for magmatic processes

Together with previous geophysical observations, our new geochemical data provide insights into the geodynamics for generation and evolution of continental intraplate basalts underneath SE China. The continuous low-velocity zone revealed by seismic tomography around 400 km depth (Huang and Zhao, 2006) could be related to deep generation of carbonatite melt through partial melt-

ing of carbonated eclogite (e.g., stagnant Pacific slab in the MTZ) (Thomson et al., 2016). When percolating through the mantle, carbonatitic melts may encounter blob or veins of CO_2-free MORB-type eclogite. Interaction of carbonatite with eclogite will result in the formation of carbonated silicate melts (Gerbode and Dasgupta, 2010). Alternatively, partial melting of carbonated eclogite embedded in the convecting mantle can also produce carbonated silicate melts (Dasgupta et al., 2006). Carbonated silicate melts reacting with a subsolidus peridotitic matrix (Xu et al., 2020b) or mixing with low-degree melts of peridotite can both produce low-silica alkali basalt. The higher Zn isotopic ratios and moderately enriched Sr-Nd isotopic signature of the low-silica samples (Fig. 4), the negative correlations of SiO_2 contents and Sr isotopic ratios with Zn isotopic ratios for the high-silica samples (Figs. 4b, 5a), as well as the positive correlations of La/Yb, Dy/Yb and Nd isotopic ratios with Zn isotopic ratios of the high-silica samples (Figs. 4c, 5b), all indicate that the geochemical signatures with strongest affinities to the carbonated eclogite component are primarily sampled by the low-silica melts generated at the deepest melting depths.

With decompression, the carbonated eclogite will be eventually exhausted, resulting in dampening the carbonated eclogite signature with an increasing contribution of melts derived from the depleted mantle. In contrast, subduction-fluid markers are most striking in the high-silica samples from the shallowest equilibrium depths. This is achieved by melting the overlying subduction-modified lithospheric mantle during further decompression.

Despite our self-consistent model of the mantle melting process, fundamental questions remain concerning the causes for mantle upwelling and the spatial and temporal distribution of basaltic volcanism. Eastern China is characterized by zero "extension rate", excluding extensional tectonics as the primary trigger for melt generation and evolution in SE China (Niu, 2005). There is, however, abundant evidence for variations of the lithospheric thickness beneath eastern China. Geophysical observations revealed that the present-day thickness of lithosphere in SE China increases suddenly from the coastline (~80 km for the high-silica samples) though the middle zone (~100 km for the low-silica samples) toward the continental interior (~190 km) (Deng et al., 2021; Yang et al., 2021b). This edge-like LAB underneath SE China may facilitate the formation of high mantle flux small-scale convection cell at the base of the lithosphere (King and Anderson, 1998), with a length scale comparable with the spatial distribution of Cenozoic basalts in SE China. The variation of the lithosphere thickness would induce eastward flow of the asthenosphere from underneath western thicker lithosphere to eastern thinner lithosphere (Niu, 2005). In addition, small-scale convection can not only facilitate decompression melting of the upwelling mantle, but also erode and melt the bottom of lithosphere (e.g., Van Wijk et al., 2010). This three-dimensional geodynamic scenario provides a bond connecting current geophysical observations of lithospheric thickness, transition from petrologically low-silica samples to high-silica samples, the spatial and temporal progressions of the magmatic activity from west to east and the P-T estimate for melt generation. Emplacement of these magmas is further facilitated by translithospheric faults, which may act as pathways for melt transport.

5. CONCLUSIONS

Cenozoic continental intraplate basalts in Zhejiang area, SE China show temporal-spatial-chemical variations and can be divided into early-stage low-silica and late-stage high-silica groups. Edge-driven small-scale convection induced by variations of the lithospheric thickness could be responsible for generating these continental intraplate basalts. Mixing of carbonated eclogite melt with low-degree melt of peridotite in the asthenosphere can produce the low-silica nephelinites and basanites observed during the early stage of magmatism, and also explains their coupled high Zn-Sr-Nd isotopic signal. Further decompression and mixing with melts derived from the sub-continental lithospheric mantle at depths approaching the LAB can result in silica-richer basanites and alkali basalts at a later stage and also explains their decoupled Zn-Sr-Nd isotopic signature. In addition, our results highlight that 1) the coupled enriched Zn-Sr-Nd isotopic signature of the carbonated eclogite component in low-silica samples can only be preserved in samples produced by low degrees of melting at the base of the melting column and 2) further decompression melting and contribution of the lithospheric mantle will mask the coupled high Zn-Sr-Nd isotopic fingerprint of carbonated eclogite and generates the apparent decoupled Zn-Sr-Nd isotopic signal in continental intraplate basalts.

Declaration of Competing Interest

The authors declare that they have no known competing financial interests or personal relationships that could have appeared to influence the work reported in this paper.

ACKNOWLEDGMENTS

We thank Ganglan Zhang for helpful discussion of Zn isotopic fractionation. Lucy McGee is thanked for her informal constructive comments and suggestions. We appreciate Sonja Aulbach and two anonymous reviewers and the editor Rosemary Hickey-Vargas for thorough and helpful comments that greatly improved the quality of this manuscript. This research was supported by the Key R&D Program of China (2019YFA0708400), the National Natural Science Foundation of China (41530211, 41903035 and 42173051), the MOST Special Fund from the State Key Laboratory of Geological Processes and Mineral Resources (CUG, MSFGPMR21 and MSFGPMR01), the China Postdoctoral Science Foundation funded project (2019M652732) and the Fundamental Research Funds for the Central Universities.

APPENDIX A. SUPPLEMENTARY MATERIAL

Supplementary data to this article can be found online at https://doi.org/10.1016/j.gca.2022.03.014.

REFERENCES

An M. and Shi Y. (2006) Lithospheric thickness of the Chinese continent. *Phys. Earth Planet. Inter.* **159**, 257–266.

Aulbach S., Lin A. B., Weiss Y. and Yaxley G. M. (2020) Wehrlites from continental mantle monitor the passage and degassing of carbonated melts. *Geochem. Perspect. Lett.*, 30–34.

Barckhausen U., and Roeser H.A. (2004) Seafloor spreading anomalies in the South China Sea revisited, Continent-ocean interactions within East Asian marginal seas. AGU Washington, DC. pp. 121–125.

Beunon H., Mattielli N., Doucet L. S., Moine B. and Debret B. (2020) Mantle heterogeneity through Zn systematics in oceanic basalts: evidence for a deep carbon cycling. *Earth. Sci. Rev.* **205**, 103174.

Briais A., Patriat P. and Tapponnier P. (1993) Updated interpretation of magnetic anomalies and seafloor spreading stages in the South China Sea: Implications for the Tertiary tectonics of Southeast Asia. *J. Geophys. Res. Solid Earth* **98**, 6299–6328.

Castillo P. R. (2015) The recycling of marine carbonates and sources of HIMU and FOZO ocean island basalts. *Lithos* **216–217**, 254–263.

Chen H., Savage P. S., Teng F.-Z., Helz R. T. and Moynier F. (2013) Zinc isotope fractionation during magmatic differentiation and the isotopic composition of the bulk Earth. *Earth. Planet. Sci. Lett.* **369–370**, 34–42.

Chung S.-L., Sun S.-S., Tu K., Chen C.-H. and Lee C.-Y. (1994) Late Cenozoic basaltic volcanism around the Taiwan Strait, SE China: product of lithosphere-asthenosphere interaction during continental extension. *Chem. Geol.* **112**, 1–20.

Cullen A., Reemst P., Henstra G., Gozzard S. and Ray A. (2010) Rifting of the South China Sea: new perspectives. *Pet. Geosci.* **16**, 273–282.

Dasgupta R., Hirschmann M. M. and Smith N. D. (2007) Partial melting experiments of peridotite + CO_2 at 3 GPa and genesis of alkalic ocean island basalts. *J. Petrol.* **48**, 2093–2124.

Dasgupta R., Hirschmann M. M. and Stalker K. (2006) Immiscible transition from carbonate-rich to silicate-rich melts in the 3 GPa melting interval of eclogite + CO_2 and genesis of silica-undersaturated ocean island lavas. *J. Petrol.* **47**, 647–671.

Dasgupta R., Mallik A., Tsuno K., Withers A. C., Hirth G. and Hirschmann M. M. (2013) Carbon-dioxide-rich silicate melt in the Earth's upper mantle. *Nature* **493**, 211–215.

Deng Y., Byrnes J. S. and Bezada M. (2021) New insights into the heterogeneity of the lithosphere-asthenosphere system beneath South China from teleseismic body-wave attenuation. *Geophys. Res. Lett.* **48** e2020GL091654.

Doucet L. S., Laurent O., Ionov D. A., Mattielli N., Debaille V. and Debouge W. (2020) Archean lithospheric differentiation: Insights from Fe and Zn isotopes. *Geology* **48**, 1028–1032.

Doucet L. S., Mattielli N., Ionov D. A., Debouge W. and Golovin A. V. (2016) Zn isotopic heterogeneity in the mantle: a melting control? *Earth. Planet. Sci. Lett.* **451**, 232–240.

Falloon T. J. and Danyushevsky L. V. (2000) Melting of refractory mantle at 1.5, 2 and 2.5 GPa under anhydrous and H_2O-undersaturated conditions: implications for the petrogenesis of high-Ca boninites and the influence of subduction components on mantle melting. *J. Petrol.* **41**, 257–283.

Fan W. (1992) Destruction of aged lower lithosphere and accretion of asthenosphere mantle beneath eastern China. *Geotecton. Metall.* **16**, 171–180.

Gale A., Dalton C. A., Langmuir C. H., Su Y. and Schilling J. G. (2013) The mean composition of ocean ridge basalts. *Geochem. Geophys. Geosyst.* **14**, 489–518.

Gao S., Ling W., Qiu Y., Lian Z., Hartmann G. and Simon K. (1999) Contrasting geochemical and Sm-Nd isotopic compositions of Archean metasediments from the Kongling high-grade terrain of the Yangtze craton: evidence for cratonic evolution and redistribution of REE during crustal anatexis. *Geochim. Cosmochim. Acta* **63**, 2071–2088.

Gerbode C. and Dasgupta R. (2010) Carbonate-fluxed melting of MORB-like pyroxenite at 2 · 9 GPa and genesis of HIMU ocean island basalts. *J. Petrol.* **51**, 2067–2088.

Guo F., Wu Y., Zhang B., Zhang X., Zhao L. and Liao J. (2021) Magmatic responses to Cretaceous subduction and tearing of the paleo-Pacific Plate in SE China: an overview. *Earth Sci. Rev.* **212**, 103448.

Guo P., Niu Y., Sun P., Gong H. and Wang X. (2020) Lithosphere thickness controls continental basalt compositions: An illustration using Cenozoic basalts from eastern China. *Geology* **48**, 128–133.

Halliday A. N., Lee D.-C., Tommasini S., Davies G. R., Paslick C. R., Fitton J. G. and James D. E. (1995) Incompatible trace elements in OIB and MORB and source enrichment in the sub-oceanic mantle. *Earth. Planet. Sci. Lett.* **133**, 379–395.

He Y., Chen L.-H., Zeng G. and Wang Z.-J. (2020) Genesis and Characteristics of Mantle Sources of Cenozoic Jiande Basalts from Zhejiang Province.. *Geological Journal of China Universities* **26**(3). doi.10.16108/j.issn1006-7493.2019043.

Herzberg C., Asimow P. D., Arndt N., Niu Y., Lesher C. M., Fitton J. G., Cheadle M. J. and Saunders A. D. (2007) Temperatures in ambient mantle and plumes: constraints from basalts, picrites, and komatiites. *Geochem. Geophys. Geosyst.*, 8.

Herzberg C., Vidito C. and Starkey N. A. (2016) Nickel–cobalt contents of olivine record origins of mantle peridotite and related rocks. *American Mineralogist* **101**, 1952–1966.

Hirose K. (1997) Partial melt compositions of carbonated peridotite at 3 GPa and role of CO_2 in alkali-basalt magma generation. *Geophys. Res. Lett.* **24**, 2837–2840.

Hirschmann M. M., Kogiso T., Baker M. B. and Stolper E. M. (2003) Alkalic magmas generated by partial melting of garnet pyroxenite. *Geology* **31**, 481–484.

Ho K.-S., Chen J.-C., Lo C.-H. and Zhao H.-L. (2003) ^{40}Ar–^{39}Ar dating and geochemical characteristics of late Cenozoic basaltic rocks from the Zhejiang-Fujian region, SE China: eruption ages, magma evolution and petrogenesis. *Chem. Geol.* **197**, 287–318.

Hoernle K., Tilton G., Le Bas M. J., Duggen S. and Garbe-Schönberg D. (2002) Geochemistry of oceanic carbonatites compared with continental carbonatites: mantle recycling of oceanic crustal carbonate. *Contrib. Mineral. Petrol.* **142**, 520–542.

Hofmann A. W. (1997) Mantle geochemistry: the message from oceanic volcanism. *Nature* **385**, 219–229.

Hong L., Xu Y.-G., Zhang L., Wang Y. and Ma L. (2020) Recycled carbonate-induced oxidization of the convective mantle beneath Jiaodong, Eastern China. *Lithos*, 366–367.

Huang J., Ackerman L., Zhang X. C. and Huang F. (2019) Mantle Zn isotopic heterogeneity caused by melt-rock reaction: evidence from Fe-rich peridotites and pyroxenites from the bohemian massif, Central Europe. *J. Geophys. Res. Solid Earth* **124**, 3588–3604.

Huang J., Chen S., Zhang X.-C. and Huang F. (2018a) Effects of melt percolation on Zn isotope heterogeneity in the mantle: constraints from peridotite massifs in Ivrea-Verbano Zone, Italian Alps. *J. Geophys. Res. Solid Earth* **123**, 2706–2722.

Huang J., Li S.-G., Xiao Y., Ke S., Li W.-Y. and Tian Y. (2015) Origin of low $\delta^{26}Mg$ Cenozoic basalts from South China Block and their geodynamic implications. *Geochim. Cosmochim. Acta* **164**, 298–317.

Huang J., Zhang X.-C., Chen S., Tang L., Wörner G., Yu H. and Huang F. (2018b) Zinc isotopic systematics of Kamchatka-

Aleutian arc magmas controlled by mantle melting. *Geochim. Cosmochim. Acta* **238**, 85–101.
Huang J. and Zhao D. (2006) High-resolution mantle tomography of China and surrounding regions. *J. Geophys. Res. Solid Earth* **1978–2012**, 111.
Huang X. and Xu Y. (2010) Thermal state and structure of the lithosphere beneath eastern China: a synthesis on basalt-borne xenoliths. *J. Earth Sci.* **21**, 711–730.
Jin Q.-Z., Huang J., Liu S.-C. and Huang F. (2020) Magnesium and zinc isotope evidence for recycled sediments and oceanic crust in the mantle sources of continental basalts from eastern China. *Lithos*, 370–371.
Kelemen P. B., Dick H. J. and Quick J. E. (1992) Formation of harzburgite by pervasive melt/rock reaction in the upper mantle. *Nature* **358**, 635–641.
Keshav S., Gudfinnsson G. H., Sen G. and Fei Y. (2004) High-pressure melting experiments on garnet clinopyroxenite and the alkalic to tholeiitic transition in ocean-island basalts. *Earth. Planet. Sci. Lett.* **223**, 365–379.
King S. D. and Anderson D. L. (1998) Edge-driven convection. *Earth. Planet. Sci. Lett.* **160**, 289–296.
Klemme S. and O'Neill H. S. (2000) The near-solidus transition from garnet lherzolite to spinel lherzolite. *Contrib. Mineral. Petrol.* **138**, 237–248.
Kogiso T. and Hirschmann M. M. (2006) Partial melting experiments of bimineralic eclogite and the role of recycled mafic oceanic crust in the genesis of ocean island basalts. *Earth. Planet. Sci. Lett.* **249**, 188–199.
Kong W., Zhang Z., Cheng Z., Liu B., Santosh M., Wei B., Ke S., Xu L. and Zhang X. (2022) Mantle source of tephritic porphyry in the Tarim Large Igneous Province constrained from Mg, Zn, Sr, and Nd isotope systematics: implications for deep carbon cycling. *GSA Bull.* **134**(1-2), 487–500.
Lambart S. (2017) No direct contribution of recycled crust in Icelandic basalts.. *Geochemical Perspectives Letters* **4**, 7–12.
Lambart S., Laporte D., Provost A. and Schiano P. (2012) Fate of pyroxenite-derived melts in the peridotitic mantle: thermodynamic and experimental constraints. *J. Petrol.* **53**, 451–476.
Lambart S., Laporte D. and Schiano P. (2009) An experimental study of pyroxenite partial melts at 1 and 1.5 GPa: Implications for the major-element composition of Mid-Ocean Ridge Basalts. *Earth. Planet. Sci. Lett.* **288**, 335–347.
Lambart S., Laporte D. and Schiano P. (2013) Markers of the pyroxenite contribution on the major-element compositions of oceanic basalts: Review of the experimental constraints.. *Lithos* **160-161**, 14–36.
Le Roux V., Dasgupta R. and Lee C. T. (2011) Mineralogical heterogeneities in the Earth's mantle: constraints from Mn Co, Ni and Zn partitioning during partial melting. *Earth. Planet. Sci. Lett.* **307**, 395–408.
Lee C.-T. A. (2004) Are Earth's core and mantle on speaking terms? *Science* **306**, 64–65.
Lee C.-T. A., Luffi P., Plank T., Dalton H. and Leeman W. P. (2009) Constraints on the depths and temperatures of basaltic magma generation on Earth and other terrestrial planets using new thermobarometers for mafic magmas. *Earth. Planet. Sci. Lett.* **279**, 20–33.
Li M.-L., Liu S.-A., Lee H.-Y., Yang C. and Wang Z.-Z. (2021) Magnesium and zinc isotopic anomaly of Cenozoic lavas in central Myanmar: origins and implications for deep carbon recycling. *Lithos*, 386–387.
Li S.-G., Yang W., Ke S., Meng X., Tian H., Xu L., He Y., Huang J., Wang X.-C., Xia Q., Sun W., Yang X., Ren Z.-Y., Wei H., Liu Y., Meng F. and Yan J. (2016) Deep carbon cycles constrained by a large-scale mantle Mg isotope anomaly in eastern China. *Natl. Sci. Rev.*, nww070.
Li X.-H., Li W.-X., Li Z.-X., Lo C.-H., Wang J., Ye M.-F. and Yang Y.-H. (2009) Amalgamation between the Yangtze and Cathaysia Blocks in South China: constraints from SHRIMP U-Pb zircon ages, geochemistry and Nd–Hf isotopes of the Shuangxiwu volcanic rocks. *Precambr. Res.* **174**, 117–128.
Li Y.-Q., Ma C.-Q., Robinson P. T., Zhou Q. and Liu M.-L. (2015) Recycling of oceanic crust from a stagnant slab in the mantle transition zone: Evidence from Cenozoic continental basalts in Zhejiang Province, SE China. *Lithos* **230**, 146–165.
Li Z.-X., Zhang L. and Powell C. M. (1995) South China in Rodinia: part of the missing link between Australia-East Antarctica and Laurentia? *Geology* **23**, 407–410.
Liao R., Zhu H., Deng J., Zhang L., Li H., Li C., Liu H. and Sun W. (2020) Zinc isotopic systematics of the South China Sea basalts and implications for its behavior during plate subduction. *Chem. Geol.*, 541.
Liu C.-Z., Wu F.-Y., Sun J., Chu Z.-Y. and Qiu Z.-L. (2012) The Xinchang peridotite xenoliths reveal mantle replacement and accretion in southeastern China. *Lithos* **150**, 171–187.
Liu S.-A. and Li S.-G. (2019) Tracing the deep carbon cycle using metal stable isotopes: opportunities and challenges. *Engineering* **5**, 448–457.
Liu S.-A., Wang Z.-Z., Li S.-G., Huang J. and Yang W. (2016a) Zinc isotope evidence for a large-scale carbonated mantle beneath eastern China. *Earth. Planet. Sci. Lett.* **444**, 169–178.
Liu S.-C., Xia Q.-K., Choi S. H., Deloule E., Li P. and Liu J. (2016b) Continuous supply of recycled Pacific oceanic materials in the source of Cenozoic basalts in SE China: the Zhejiang case. *Contrib. Mineral Petrol.*, 171.
Liu S. A., Wang Z. Z., Yang C., Li S. G. and Ke S. (2020) Mg and Zn isotope evidence for two types of mantle metasomatism and deep recycling of magnesium carbonates. *J. Geophys. Res Solid Earth*, 125.
Lu J., Zheng J., Griffin W. L., O'Reilly S. Y. and Pearson N. J. (2015) Microscale effects of melt infiltration into the lithospheric mantle: peridotite xenoliths from Xilong, South China. *Lithos* **232**, 111–123.
Lu J., Zheng J., Griffin W. L. and Yu C. (2013) Petrology and geochemistry of peridotite xenoliths from the Lianshan region: Nature and evolution of lithospheric mantle beneath the lower Yangtze block. *Gondwana Res.* **23**, 161–175.
Ma X. and Wu D. (1987) Cenozoic extensional tectonics in China. *Tectonophysics* **133**, 243–255.
Mallik A. and Dasgupta R. (2012) Reaction between MORB-eclogite derived melts and fertile peridotite and generation of ocean island basalts. *Earth. Planet. Sci. Lett.* **329–330**, 97–108.
Mallik A. and Dasgupta R. (2014) Effect of variable CO_2 on eclogite-derived andesite and lherzolite reaction at 3 GPa—implications for mantle source characteristics of alkalic ocean island basalts. *Geochem. Geophys. Geosyst.* **15**, 1533–1557.
McCoy-West A. J., Fitton J. G., Pons M.-L., Inglis E. C. and Williams H. M. (2018) The Fe and Zn isotope composition of deep mantle source regions: insights from Baffin Island picrites. *Geochim. Cosmochim. Acta* **238**, 542–562.
McDonough W. F. and Sun S. S. (1995) The composition of the Earth. *Chem. Geol.* **120**, 223–253.
McGee L. E., Smith I. E. M., Millet M.-A., Handley H. K. and Lindsay J. M. (2013) Asthenospheric control of melting processes in a monogenetic basaltic system: a case study of the Auckland Volcanic Field, New Zealand. *J. Petrol.* **54**, 2125–2153.
Moussallam Y., Longpré M.-A., McCammon C., Gomez-Ulla A., Rose-Koga E. F., Scaillet B., Peters N., Gennaro E., Paris R. and Oppenheimer C. (2019) Mantle plumes are oxidised. *Earth. Planet. Sci. Lett.*, 527.

Niu Y. (2005) Generation and evolution of basaltic magmas: some basic concepts and a new view on the origin of Mesozoic-Cenozoic basaltic volcanism in eastern China. *Geol. J. China Univ.* **11**, 9–46.

O'Hara M. J. (1968) The bearing of phase equilibria studies in synthetic and natural systems on the origin and evolution of basic and ultrabasic rocks. *Earth Sci. Rev.* **4**, 69–133.

Pertermann M. and Hirschmann M. M. (2003) Anhydrous partial melting experiments on MORB-like eclogite: phase relations, phase compositions and mineral–melt partitioning of major elements at 2–3 GPa. *J. Petrol.* **44**, 2173–2201.

Pilet S., Baker M. B. and Stolper E. M. (2008) Metasomatized lithosphere and the origin of alkaline lavas. *Science* **320**, 916–919.

Pons M. L., Debret B., Bouilhol P., Delacour A. and Williams H. (2016) Zinc isotope evidence for sulfate-rich fluid transfer across subduction zones. *Nat Commun* **7**, 13794.

Qi Q. U., Taylor L. A. and Zhou X. (1995) Petrology and Geochemistry of Mantle Peridotite Xenoliths from SE China. *J. Petrol.* **36**, 55–79.

Qiu Y. M., Gao S., McNaughton N. J., Groves D. I. and Ling W. (2000) First evidence of> 3.2 Ga continental crust in the Yangtze craton of south China and its implications for Archean crustal evolution and Phanerozoic tectonics. *Geology* **28**, 11–14.

Shi H. and Li C.-F. (2012) Mesozoic and early Cenozoic tectonic convergence-to-rifting transition prior to opening of the South China Sea. *Int. Geol. Rev.* **54**, 1801–1828.

Shu L. and Charvet J. (1996) Kinematics and geochronology of the Proterozoic Dongxiang-Shexian ductile shear zone: with HP metamorphism and ophiolitic melange (Jiangnan Region, South China). *Tectonophysics* **267**, 291–302.

Sossi P. A., Nebel O., O'Neill H. S. C. and Moynier F. (2018) Zinc isotope composition of the Earth and its behaviour during planetary accretion. *Chem. Geol.* **477**, 73–84.

Spandler C., Yaxley G., Green D. H. and Rosenthal A. (2008) Phase relations and melting of anhydrous K-bearing eclogite from 1200 to 1600 C and 3 to 5 GPa. *J. Petrol.* **49**, 771–795.

Suhr N., Schoenberg R., Chew D., Rosca C., Widdowson M. and Kamber B. S. (2018) Elemental and isotopic behaviour of Zn in Deccan basalt weathering profiles: chemical weathering from bedrock to laterite and links to Zn deficiency in tropical soils. *Sci. Total Environ.* **619**, 1451–1463.

Sun P., Niu Y., Guo P., Ye L., Liu J. and Feng Y. (2017) Elemental and Sr–Nd–Pb isotope geochemistry of the Cenozoic basalts in Southeast China: Insights into their mantle sources and melting processes. *Lithos* **272–273**, 16–30.

Takahashi E. and Kushiro I. (1983) Melting of a dry peridotite at high pressures and basalt magma genesis. *Am. Mineral.* **68**, 859–879.

Takahashi E. and Scarfe C. M. (1985) Melting of peridotite to 14 GPa and the genesis of komatiite. *Nature* **315**, 566–568.

Takahashi E., Shimazaki T., Tsuzaki Y. and Yoshida H. (1993) Melting study of a peridotite KLB-1 to 6.5 GPa, and the origin of basaltic magmas. *Philos. Trans. R. Soc. London Ser. A* **342**, 105–120.

Tapponnier P., Peltzer G. and Armijo R. (1986) On the mechanics of the collision between India and Asia. *Geo. Soc. London Special Pub.* **19**, 113–157.

Tapponnier P., Peltzer G., Le Dain A., Armijo R. and Cobbold P. (1982) Propagating extrusion tectonics in Asia: new insights from simple experiments with plasticine. *Geology* **10**, 611–616.

Tatsumoto M., Basu A. R., Wankang H., Junwen W. and Guanghong X. (1992) Sr, Nd, and Pb isotopes of ultramafic xenoliths in volcanic rocks of Eastern China: enriched components EMI and EMII in subcontinental lithosphere. *Earth. Planet. Sci. Lett.* **113**, 107–128.

Taylor B. and Hayes D. E. (1980) The tectonic evolution of the South China Basin. In *The tectonic and geologic evolution of Southeast Asian seas and islands* (ed. D. E. Hayes). AGU, Washington, D.C., pp. 89–104.

Taylor B. and Hayes D. E. (1983) Origin and history of the South China Sea basin. In *The tectonic and geologic evolution of Southeast Asian seas and islands: Part 2* (ed. D. E. Hayes). AGU, Washington, D.C., pp. 23–56.

Thomson A. R., Walter M. J., Kohn S. C. and Brooker R. A. (2016) Slab melting as a barrier to deep carbon subduction. *Nature* **529**, 76–79.

Tsuno K. and Dasgupta R. (2011) Melting phase relation of nominally anhydrous, carbonated pelitic-eclogite at 2.5–3.0 GPa and deep cycling of sedimentary carbon. *Contrib. Mineral. Petrol.* **161**, 743–763.

Van Wijk J., Baldridge W., Van Hunen J., Goes S., Aster R., Coblentz D., Grand S. and Ni J. (2010) Small-scale convection at the edge of the Colorado Plateau: implications for topography, magmatism, and evolution of Proterozoic lithosphere. *Geology* **38**, 611–614.

Walter M. J. (1998) Melting of garnet peridotite and the origin of komatiite and depleted lithosphere. *J. Petrol.* **39**, 29–60.

Wang S.-J., Teng F.-Z. and Scott J. M. (2016) Tracing the origin of continental HIMU-like intraplate volcanism using magnesium isotope systematics. *Geochim. Cosmochim. Acta* **185**, 78–87.

Wang S. and Yan J. (2021) Coexisting Early Cretaceous arc-type and OIB-type mafic magmatic rocks in the eastern Jiangnan Orogen, South China Block: Implications for paleo-Pacific plate subduction. *Lithos* **400–401**, 106421.

Wang W., Zhou M.-F., Yan D.-P., Li L. and Malpas J. (2013) Detrital zircon record of Neoproterozoic active-margin sedimentation in the eastern Jiangnan Orogen. *South China. Precambrian Res.* **235**, 1–19.

Wang Z.-Z. and Liu S.-A. (2021) Evolution of intraplate alkaline to tholeiitic basalts via interaction between carbonated melt and lithospheric mantle. *J. Petrol.* **62**, 1–25.

Wang Z.-Z., Liu S.-A., Chen L.-H., Li S.-G. and Zeng G. (2018) Compositional transition in natural alkaline lavas through silica-undersaturated melt–lithosphere interaction. *Geology* **46**, 771–774.

Wang Z.-Z., Liu S.-A., Liu J., Huang J., Xiao Y., Chu Z.-Y., Zhao X.-M. and Tang L. (2017) Zinc isotope fractionation during mantle melting and constraints on the Zn isotope composition of Earth's upper mantle. *Geochim. Cosmochim. Acta* **198**, 151–167.

Workman R. K. and Hart S. R. (2005) Major and trace element composition of the depleted MORB mantle (DMM). *Earth. Planet. Sci. Lett.* **231**, 53–72.

Wyllie P. J. and Huang W.-L. (1976) Carbonation and melting reactions in the system CaO–MgO–SiO2–CO2 at mantle pressures with geophysical and petrological applications. *Contrib. Mineral. Petrol.* **54**, 79–107.

Xu R., Liu Y. and Lambart S. (2020a) Melting of a hydrous peridotite mantle source under the Emeishan large igneous province. *Earth Sci. Rev.* **207**, 103253.

Xu R., Liu Y., Wang X.-C., Foley S. F., Zhang Y. and Yuan H. (2020b) Generation of continental intraplate alkali basalts and implications for deep carbon cycle. *Earth Sci. Rev.* **201**, 103073.

Xu Y., Li H., Hong L., Ma L., Ma Q. and Sun M. (2018) Generation of Cenozoic intraplate basalts in the big mantle wedge under eastern Asia. *Sci. China Earth Sci.* **61**, 869–886.

Xu Y.-G., Ma J.-L., Frey F. A., Feigenson M. D. and Liu J.-F. (2005) Role of lithosphere–asthenosphere interaction in the genesis of Quaternary alkali and tholeiitic basalts from Datong, western North China Craton. *Chem. Geol.* **224**, 247–271.

Yang C., Liu S.-A., Zhang L., Wang Z.-Z., Liu P.-P. and Li S.-G. (2021a) Zinc isotope fractionation between Cr-spinel and olivine and its implications for chromite crystallization during magma differentiation. *Geochim. Cosmochim. Acta* **313**, 277–294.

Yang C. and Liu S. A. (2019) Zinc isotope constraints on recycled oceanic crust in the mantle sources of the Emeishan large igneous province. *J. Geophys. Res. Solid Earth* **124**(12), 12537–12555.

Yang X., Li Y., Afonso J. C., Yang Y. and Zhang A. (2021b) Thermochemical State of the Upper Mantle Beneath South China From Multi-Observable Probabilistic Inversion. *J. Geophys. Res. Solid Earth*, 126.

Yang Z. F., Li J., Jiang Q. B., Xu F., Guo S. Y., Li Y. and Zhang J. (2019) Using Major Element Logratios to Recognize Compositional Patterns of Basalt: Implications for Source Lithological and Compositional Heterogeneities. *J. Geophys. Res. Solid Earth* **124**, 3458–3490.

Ye M.-F., Li X.-H., Li W.-X., Liu Y. and Li Z.-X. (2007) SHRIMP zircon U-Pb geochronological and whole-rock geochemical evidence for an early Neoproterozoic Sibaoan magmatic arc along the southeastern margin of the Yangtze Block. *Gondwana Res.* **12**, 144–156.

Yu X., Chen L.-H. and Zeng G. (2015) Growing magma chambers control the distribution of small-scale flood basalts. *Sci. Rep.*, 5.

Yu X., Chen L.-H. and Zeng G. (2017) Magmatic recharge buffers the isotopic compositions against crustal contamination in formation of continental flood basalts. *Lithos* **284–285**, 1–10.

Zeng G., Chen L.-H., Xu X.-S., Jiang S.-Y. and Hofmann A. W. (2010) Carbonated mantle sources for Cenozoic intra-plate alkaline basalts in Shandong, North China. *Chem. Geol.* **273**, 35–45.

Zeng G., He Z.-Y., Li Z., Xu X.-S. and Chen L.-H. (2016) Geodynamics of paleo-Pacific plate subduction constrained by the source lithologies of Late Mesozoic basalts in southeastern China. *Geophys. Res. Lett.* **43**, 10,189–110,197.

Zeng G., Zheng L., Chen L., Liu J., Zhang H., Zhang Y. and Shi J. (2017) Influence of ridge suction on Cenozoic basaltic magmatism in the surroundings of the South China Sea. *Geol. J. China Univ.* **23**, 373–382 (In Chinese with English abstract).

Zhang G.-L., Chen L.-H., Jackson M. G. and Hofmann A. W. (2017) Evolution of carbonated melt to alkali basalt in the South China Sea. *Nat. Geosci.* **10**, 229–235.

Zhang H., Zheng J., Lu J., Lin A., Zhou Y. and Zhao Y. (2021) Nature and evolution of the lithospheric mantle beneath the South China. *Lithos*, 398–399.

Zhao G. and Cawood P. A. (2012) Precambrian geology of China. *Precambrian Res.* **222–223**, 13–54.

Zheng J. P., Lee C. T. A., Lu J. G., Zhao J. H., Wu Y. B., Xia B., Li X. Y., Zhang J. F. and Liu Y. S. (2015) Refertilization-driven destabilization of subcontinental mantle and the importance of initial lithospheric thickness for the fate of continents. *Earth. Planet. Sci. Lett.* **409**, 225–231.

Zhou X., Sun T., Shen W., Shu L. and Niu Y. (2006) Petrogenesis of Mesozoic granitoids and volcanic rocks in South China: a response to tectonic evolution. *Episodes* **29**, 26.

Zou H., Zindler A., Xu X. and Qi Q. (2000) Major, trace element, and Nd, Sr and Pb isotope studies of Cenozoic basalts in SE China: mantle sources, regional variations, and tectonic significance. *Chem. Geol.* **171**, 33–47.

Associate editor: Rosemary Hickey-Vargas